Repetitive Late Pleistocene soft-sediment deformation by seismicity-induced liquefaction in north-western Lithuania

Szymon Belzyt[1*], Małgorzata Pisarska-Jamroży[1], Albertas Bitinas[2,3], Barbara Woronko[4], Emrys R. Phillips[5], Jan A. Piotrowski[6,7], Asta Jusienė[8]

[1]Institute of Geology, Adam Mickiewicz University, B. Krygowskiego 12, 61-680 Poznań, Poland; e-mail: szymon.belzyt@amu.edu.pl, pisanka@amu.edu.pl; https://orcid.org/0000-0002-1633-40354035;

[2]Nature Research Centre, Akademijos 2, LT-08412 Vilnius, Lithuania; e-mail: albertas.bitinas@gamtc.ku.lt

[3]Marine Research Institute, Klaipėda University, Universiteto av. 17, LT-92294 Klaipėda, Lithuania; e-mail: albertas.bitinas@apc.ku.lt

[4]University of Warsaw, Faculty of Geology, Żwirki i Wigury 93, 02-089 Warsaw, Poland; e-mail: bworonko@uw.edu.pl

[5]British Geological Survey, The Lyell Centre, Research Avenue South, Edinburgh, EH14 4AP, UK; e-mail: erp@bgs.ac.uk

[6]Department of Geoscience, Aarhus University, Høegh-Guldbergs Gade 2, DK-8000 Aarhus C, Denmark; e-mail: jan.piotrowski@geo.au.dk

[7]Faculty of Earth Sciences, Nicolaus Copernicus University, Lwowska 1, 87-100 Toruń, Poland

[8]Lithuanian Geological Survey, S. Konarskio 35, Vilnius LT-03123, Lithuania; e-mail: asta.jusiene@lgt.lt

*Corresponding author

ABSTRACT

Liquefaction can cause deformation of unconsolidated sediment, but specific processes involved and the trigger mechanisms often remain obscured. This study describes multiple internally deformed sediment layers in a succession of lacustrine sand, silt and clay deposited during the Marine Isotope Stage 5d in north-western Lithuania. The deformation structures (load casts, pseudonodules, ball-and-pillow structures, broken-up laminae, and injections) are embedded in separate layers of fine-grained, laterally continuous sediments. Detailed meso- and micro-scale sedimentological analyses suggest that each deformation event consisted of numerous successive stages of sediment advection facilitated by liquefaction. Low-permeability fine-grained laminae contributed to localized pore-water pressure build-up and lowering of sediment strength. Truncation surfaces on top of layers that limit layers with soft-sediment deformation structures (SSDS) suggest that the deformation events were separated by repetitive periods of erosion and uninterrupted deposition in the lake. The most likely trigger of the deformation was recurrent palaeoseismic activity possibly linked to a late glacial isostatic adjustment following the Scandinavian Ice Sheet melting after the Saalian glaciation in the area. This study not only emphasizes the potential role of seismic processes in shaping the sedimentary record of the intraplate region of north-eastern Europe, but also contributes to constraining the depth of liquefaction, regardless of the actual trigger mechanism.

Keywords: soft-sediment deformation structures, injection structures, load structures, palaeosurfaces, seismites, microstructural analysis, Quaternary

INTRODUCTION

Soft-sediment deformation structures (SSDS) may develop under various environmental conditions in unconsolidated, water-saturated deposits leading to disharmonic folding and disruption of these sediments during or shortly after deposition (e.g. Allen, 1982a), often facilitated by liquefaction. Most prone to liquefaction are loosely packed silty and fine-grained sandy deposits (cf. Obermeier, 1996; Vanneste *et al.*, 1999). Deciphering the trigger mechanism and the driving force of this type of deformation in different sedimentary environments is still a timely issue in the field of Quaternary geology, sedimentology and tectonics, especially in formerly-glaciated intraplate stable continental core regions of the Northern Hemisphere (e.g. Van Vliet-Lanoë *et al*., 2004; Brandes & Winsemann, 2013; Van Loon et al., 2016; Brooks, 2018; Brandes *et al*., 2018; Pisarska-Jamroży *et al*., 2018a, 2019a; Bertran *et al*., 2019; Grube, 2019; Brooks & Adams, 2020; Van Loon *et al,*, 2020 and references therein). Recently, research focused on distinguishing between seismic and non-seismic triggers based on SSDS and their position within the sedimentary record (e.g. Wheeler, 2002; Menzies & Taylor, 2003; Van Vliet-Lanoë *et al*., 2004; Horváth *et al*., 2005; Owen & Moretti, 2008, 2011; Alsop & Marco, 2011; Owen *et al.*, 2011; Van Loon & Maulik, 2011; Brandes & Winsemann, 2013; Moretti & Van Loon, 2014; Pisarska-Jamroży *et al*., 2018a, 2019a; Bertran *et al*., 2019; Van Loon *et* al., 2020; Zhong *et al*., 2020). Microstructural and microsedimentological investigation of SSDS can help to recognize deformation induced by palaeoearthquakes by identifying (1) postdepositional microstructures attributable to seismic processes (Menzies & Taylor, 2003; Vanneste *et al.*, 2008; Menzies & van der Meer, 2018; Giona Bucci *et al.*, 2019), (2) “seismic event horizons” (Vanneste *et al.*, 2008; Giona Bucci *et al.*, 2019), (3) specific surface microtextures of individual grains and crushed grains (Mahaney *et al.*, 2004) or (4) palaeoliquefaction features that differ from modern liquefaction features (Giona Bucci *et al.*, 2019).

One of the characteristic features of sediments affected by seismicity-induced liquefaction is the vertical repetition of laterally continuous deformed layers interbedded with undeformed sediments, called “sandwich-like distribution” (Hilbert-Wolf *et al*., 2009 and references therein; Owen & Moretti, 2011; Van Loon *et al.*, 2016; Morsilli *et al.*, 2020). This vertical repetition, among other criteria, has been used to identify seismites both in tectonically active interplate areas (e.g. Sims, 1975; Gibert *et al.*, 2011; Alsop & Marco, 2011; Alsop *et al.*, 2019; Morsilli *et al.*, 2020) and in intraplate regions of low-seismicity (e.g. Van Loon *et al.*, 2016; Pisarska-Jamroży *et al.*, 2018a, 2019a; Pisarska-Jamroży & Woźniak, 2019). The majority of liquefaction features occur at depths between 1 and 10 m below the past ground surface (palaeosurface), often at depths between 2 and 4 m (Obermeier, 1996, 2009; Obermeier *et al*., 2002; Towhata *et al*., 2014), and are commonly restricted to the uppermost few decimetres making them readily accessible for observation. Nevertheless, unequivocal sedimentological proxies of the episodic, time-transgressive nature of soft-sediment deformation and the position of liquefied sediments within the succession during the recurring deformation events are still largely lacking.

The paper describes a 4.5-m thick sediment succession containing ten layers with exceptionally well-developed SSDS of various types in the Late Pleistocene lacustrine deposits exposed at the Dyburiai study site in NW Lithuania. The occurrence of multiple deformed layers, with variable types of SSDS and differentiated types of bases and tops, over a short distance at the Dyburiai outcrop, is an excellent comparative feature for the reconstruction of a number of liquefaction events, what thus can help in estimation of the possible recurrence of deforming events in all palaeoenvironments. The main objective of the study is to constrain the environmental conditions that facilitated the formation of SSDS with focus on the actual trigger mechanism. We aim to explain the possible impact of the properties of host sediments on the style and relative intensity of deformation, and identify the depth of sediments affected by liquefaction, which is novel in the studies of such sediments.

GEOLOGICAL SETTING

The study area is located in the south-western part of the East European Craton composed of more than 2-km-thick Phanerozoic sediment cover overlying the Precambrian crystalline basement. The area is considered as a seismically inactive, stable continental core region. However, two M=5 and M=5.2 earthquakes that occurred in 2004, with epicentre in the Kaliningrad District of Russia (Gregersen *et al.*, 2007), and some lower-magnitude seismic activities have been recorded or interpreted from instrumental and historical records (Pačėsa & Šliaupa, 2011; Lazauskienė *et al.*, 2012; Nikulins, 2017; Nikulins & Assinovskaya, 2018). The seismic activity is related to deeply-rooted pre-Quaternary faults in bedrock, off which the most prominent is the W-E striking Telšiai fault zone.

The study area is located in the Western Samogitia Plain, NW Lithuania (Fig. 1A and B). This area was overridden several times by the Scandinavian Ice Sheet during the Elsterian, Saalian and Late Weichselian glaciations (Guobytė & Satkūnas, 2011) that left behind a complex succession of several till units separated by glaciofluvial sand and lacustrine sand, silt and clay. The surface geology in the study area consists mainly of water-laid deposits of the Late Weichselian (Upper Nemunas) age that form a hummocky terrain created during the final stages of the last deglaciation (Guobytė, 2000).

The Dyburiai outcrop (Fig. 1B) is situated in the middle course of the Minija River, a tributary of the Nemunas River. The lateral extent of the outcrop is limited by Holocene slope deposits, vegetation and a thick talus that cover the adjacent slopes of the steeply-incised, 33-m-deep river valley (Fig. 2).

METHODS

The sediments at the Dyburiai site were logged in three vertical profiles at key points across the exposed section in order to investigate lateral variations in the sedimentary architecture and constrain changes in the style and intensity of the deformation. Textural and structural characteristics of the sediments were described using a lithofacies approach of Miall (1977) modified by Zieliński & Pisarska-Jamroży (2012).

Sixteen samples were collected for grain size analysis; two from each of the eight sampled layers with SSDS, one from the injected sediments, and one from adjacent loaded sediments. The grain size distribution was determined by laser diffractometry processed with GRADISTAT 8.0 software. The basic statistic parameters were determined using the logarithmic method of Folk & Ward (1957).

Mesoscale structural features (orientation of the fault planes and the fault offsets) were measured in the field. The results are projected on contoured lower hemisphere stereonets with the mean fault plane orientations and principle stress directions calculated with Stereonet 10 software.

Four samples were collected for optically stimulated luminescence (OSL) dating using 25-cm long, opaque plastic tubes protecting the sample from exposure to sunlight. The samples were collected from undeformed, ripple cross-laminated (lowermost part of unit 3; two samples) and horizontally-laminated (uppermost part of unit 3; two samples) sand (Fig. 3). The dating was performed at the GADAM Gliwice Luminescence Laboratory using the standard multi-grain aliquots method applied to coarse-grained (90–125 μm) quartz. Equivalent doses of samples were determined using the single-aliquot regenerative-dose (SAR) protocol and the age estimates were obtained using the Central Age Model.

Four undisturbed oriented samples were collected from the sediment layers containing SSDS. Two of the samples were taken from the upper part of layer SSDS-1 (sample Di1A at the bottom and Di1B at the top), one sample from SSDS-3 (sample Di3; comprising the whole vertical extent of the layer), and one sample from SSDS-10 (sample Di10; see Fig. 3). Thin sections (6x9 cm) were analysed to provide detailed insights in the deformation and injection structures to facilitate reconstruction of the processes accompanying the deformation.

Microstructural and microsedimentological analysis was conducted using high-resolution images from Nikon Eclipse LV100 polarization microscope (plane-polarized light) with motorized XY stage and camera, as well as high resolution scans from Epson V37 device.

Till fabric analysis (100 measurements in each point) and petrographic analysis of gravel fraction (5–10 mm; 300 pebbles in each sample) in these tills were carried out during the geological mapping by the Lithuanian Geological Survey and the results have been reported earlier by Jusienė (2012) and Pisarska-Jamroży *et al*. (2018b).

SEDIMENTARY SUCCESSION

The Dyburiai section is 32 m high and 35 m wide. The exposed sedimentary succession is divided into four key units (Fig. 3A).

Description

Unit 1

The lowermost unit (unit 1; Fig. 3A) is a 15-m thick succession comprising three diamictons (lithofacies Dm) characterized by relatively similar petrographic compositions (21–36% crystalline rocks, 5–6% sandstones and quartzites, 6–14% dolomites, 7–32% marls, and 32–45% limestones; Fig. 3A) and a dominant NE-SW orientation of clasts macrofabrics. The diamictons are separated by beds of massive, fine-grained sand and massive silt (lithofacies Sm and Tm, Fig. 3) (Jusienė, 2012; Pisarska-Jamroży *et al.*, 2018b). These data do not allow more detailed stratigraphic subdivision and all these deposits are preliminarily considered as a single lithostratigraphic unit (complex) formed during one glacial cycle.

Unit 2

Unit 2 (Fig. 3A) crops out between 54.5-59.5 m a.s.l. and comprises a coarse-grained succession of massive gravel (Gm), sandy gravel (GSm) and coarse-grained sand (Sm). The massive gravel and sandy gravel consist of well-rounded pebbles and coarse-grained sand. The massive sandy lithofacies is composed of coarse- to medium-grained sand.

Unit 3

Unit 3 (Fig. 3A) occurs between 59.5 and 64 m a.s.l. and is composed of deformed fine-grained sandy and silty sediments (lithofacies Sd, SFd, FSd, Fd), but also undeformed ripple-cross laminated, horizontally laminated sand (lithofacies Sr, Sh), wavy-laminated fines (lithofacies Fw), massive sand, and massive fines (lithofacies Sm, Fm, Mm). Erosional features and clay clasts are widespread in the upper parts of the beds containing SSDS. The thicknesses of individual lithofacies range from few up to 55 centimetres. The OSL dates indicate that the lower part of unit 3 was deposited between 111.9±7.8 ka (GdTL-2864) and 105.0±7.1 ka (GdTL-2865) and the upper part between 101.9±7.4 ka (GdTL-2866) and 98.7±7.6 ka (GdTL-2867) (Fig. 3A and supplementary figures 1 and 2). A detailed description of this unit is provided in section "Deformations in unit 3".

Unit 4

The uppermost part of the succession (Fig. 3A) consists of an 8-m thick diamicton (lithofacies Dm) containing large (0.1 to 1.1 m long) lenticular clasts of sand and silt which are partially deformed by shear planes, thrust faults, small-scale folds and flexures. The clast macrofabrics measured in three places along the vertical profile of this unit show preferred NW-SE and NNW-SSE clast orientations, consistent with ice advancing from NW-NNW. The clasts within the diamicton are composed of 29–42% crystalline rocks, 6–18% sandstones and quartzites, 39–43% limestones, up to 14% dolomites, and few or no marls (Pisarska-Jamroży *et al.*, 2018b).

Interpretation

Unit 1

Based on the petrographic composition and clast microfabrics, the three lower diamictons of unit 1areinterpreted as tills. Together with the interbedded sand and silt, the tills were deposited during the Saalian glaciation (Marine Isotope Stage MIS 6) according to Guobytė & Satkūnas (2011).

Unit 2

The coarser-grained sediments of unit 2 were deposited by highly energetic glaciofluvial rivers during the retreat of the Saalian ice sheet (MIS 6). All lithofacies indicates non-channelized quite shallow, flashy currents of sheet flood type (cf. McKee *et al.*, 1967; Miall, 1977; Pisarska-Jamroży, 2008; Pisarska-Jamroży & Zieliński, 2014) in the upper flow regime (Harms *et al.*, 1982), with plane-bed accretion. Gravels and sandy gravels can be attributed to flood-flow pulses terminating in waning-flow sandy deposits. Such flows could exist in the upper part of a terminoglacial fan (Zieliński & Van Loon, 1999).

Unit 3

This unit derives from deposition of fine-grained silty and sandy sediments in a low-energy lacustrine environment. The massive and horizontally laminated silt and fine sand were deposited from suspension fallout, while the ripple cross-laminated sand records a periodic input of slightly coarser grained sediment by small-volume inflows (cf. Pisarska-Jamroży, 2013 and references therein). The presence of erosional surfaces with small-scale troughs and clay laminae disrupted by currents, immediately underlying the ripple-cross laminated sand documents increasing current activity within the lake prior to, or during the deposition of this sand. The semi-rhythmic nature of the sediments indicates phases of deposition in slow flowing water (silty sediments) and deposition from currents (sandy ripple marks). Such changes likely occurred in a lake periodically fed by inflows. OSL ages in all four samples in unit 3 become younger upward in the succession. The time span of the lacustrine deposition was likely between 111.9±7.8 ka and 98.7±7.6 ka, an age range consistent with the regional stratigraphy. This period corresponds with the colder part of MIS 5 (cf. Gibbard & Lewin, 2016) but at that time Lithuania has not been glaciated (Guobytė & Satkūnas, 2011).

Unit 4

The upper, thick diamicton characterised by petrographic composition different from the diamictons in unit 1 (Guobytė & Satkūnas, 2011), is interpreted as a subglacial traction till or glacitectonite containing deformed clasts of pre-existing sediments. This till was most probably deposited during the Late Weichselian (Upper Nemunas) advance of the Scandinavian Ice Sheet (Pisarska-Jamroży *et al.*, 2018b).

DEFORMATIONS IN UNIT 3

Layers with SSDS

Ten layers with an exceptionally rich SSDS assemblage occur in the 5-m-thick lacustrine part of the study site (unit 3; Figs 3 and 4). Most of the identified SSDS (injections, load structures; see Figs 4 and 5; Table 1) are found within distinct layers coded SSDS-1 to SSDS-10 separated by and often interbedded with undeformed sediments, which together yield a pancake appearance (Fig. 4). All SSDS layers apart from SSDS-2 are laterally continuous along the whole section, they typically have constant thicknesses and sharp, mostly erosional tops and gradational bases (Figs 2B, 3B and 4; Table 1).

Characteristics of layers with SSDS

SSDS-1

SSDS-1 is the lowermost deformation layer in unit 3. It is typically 45 to 50 cm thick, but gradually thins towards the north where it is only 25 to 30 cm thick (Table 1; Figs 2B and 6D). The bottom contact with ripple-cross laminated sand is gradational, while the top is sharp and erosive (Fig. 6D and E). The uppermost part contains clay fragments derived from a thin clay laminae (Fig. 6D). The sizes and shapes of the internally highly deformed load structures in layer SSDS-1 are extremely variable (Table 1; Figs 6D and F to H). Locally, in the central part of the section, ripple-cross laminated sands underlying the clay laminae form load structures (type C) with well-preserved internal lamination (Figs 5 and 6E) reflecting a spatially variable intensity of deformation of this originally thinly bedded to laminated sand and silt. The load casts generally decrease in sizes towards NE in parallel with the overall thickness decrease of this layer.

SSDS-2

Layer SSDS-2 only occurs in the NE part of the section and thins towards SW (Fig. 2B). Where present, this layer occurs approximately 20-35 cm above layer SSDS-1 and is separated from it by undeformed ripple cross-laminated sand and silt. Layer SSDS-2 is up to 25 cm thick with gradational base and erosional top. The intensity of deformation in SSDS-2 is less than in SSDS-1, with only the uppermost 15 cm affected. Prior to deformation, layer SSDS-2 comprised a thinly laminated succession of ripple-cross laminated fine sand and silty sand, locally separated by thin (3 mm) clay laminae (Fig. 7D).

SSDS-3 and SSDS-4

The closely spaced layers SSDS-3 and -4 are between 5 and 7 cm thick. They are separated by an up to 1-cm thick layer of massive silty clay (Fig. 6F). The bases of layers SSDS-3 and SSDS-4, as well as the top of layer SSDS-3, are gradational, but the contact of layer SSDS-4 with the overlying ripple cross-laminated sand is erosional (Table 1). In both layers similar style of deformation occurs (Table 1). The thicknesses of these layers and the sizes of individual deformation structures are smaller than in other SSDS layers. Towards the NE part of the section, the deformation structures are less frequent and in the outermost 4 m of the outcrop they merge into a single layer. The underlying silty/clayey laminae splits and plunges down into fine sand and silty sand delimiting the top of layer SSDS-2.

SSDS-5 and SSDS-6

Layers SSDS-5 and SSDS-6 are directly superposed (Figs 4A to B and 6B). In both layers, regularly distributed load casts and injection structures are widespread (Table 1). The base of layer SSDS-5 is erosional and its top is gradational, while the base of layer SSDS-6 is gradational and its top – erosional (Table 1). In the SW part of the section, two injections rooted in the earlier deformed SSDS-5 cut the overlying SSDS-6 and end in ripple cross-laminated sand (Fig. 7A and B). This suggests multiple stages of deformation in a single progressive event that happened without any long-lasting breaks.

SSDS-7

Layer SSDS-7 is the most coarse-grained unit within the whole lacustrine sediment succession (Fig. 7). Its thickness varies from 10 cm to 35 cm (Table 1, Figs 2 and 4A). Its top occasionally contains erosional features (Table 1). The load casts and flame structures of variable sizes and shapes found here are distributed chaotically both in the horizontal and vertical direction in the layer. Distinct load casts occur in the lower part of the layer while the upper part is more homogenous (Fig. 6G). Several generations of deformation structures visible in the internal lamination within the load casts suggest a complex, multi-phase style of deformation (upper part of Fig. 7A and B). Although the grain size difference between the deformed load casts and the undeformed host sediment is small, preferential loading of sand into silty sand is observed (see Fig. 8).

SSDS-8

The thickness of layer SSDS-8 is between 10 cm to 25 cm (Table 1). Its top contact is sharp and eroded by sandy ripples. Vertical injection structures deformed and pulled upward the fragmented fine-grained laminae as indicated by the long axes of folds in these laminae oriented parallel to the injection structures (Fig. 9C).

SSDS-9

The thickness of layer SSDS-9 is constant along the entire outcrop. The bottom of the layer SSDS-9 is gradational, while its top is erosional. The original sediment in this layer was most probably laminated silt and sand. Flat-bottomed small-scale ball-and-pillow structures occur in the layer.

SSDS-10

The distinct feature of layer SSDS-10 is randomly distributed small-scale (up to 1 cm) pseudonodules that are most frequent in the upper part (Figs 9B and 10B). The top is erosional (Fig. 3B). Locally in the uppermost part of SSDS-10 load casts of various sizes and shapes (from complex to drop-like) occur (Fig. 6B). They were probably formed in small erosional hollows in the top part of the silty layer.

Interpretation of SSDS layers

The sandwich-like (pancake-like) arrangement of layers SSDS-1 to SSDS-10 with mostly erosional features at their tops suggests that a single deformational event impacted each individual layer. As suggested by Anketell *et al.* (1969, 1970) some of the planar upper surfaces of layers with SSDS (Fig. 6A, B, D) called 'unconformable surfaces', might have been formed by redistribution of liquefied and/or fluidised sediment following the main deformation event in the absence of current erosion. However, tops of the layers at Dyburiai study site are not planar, but scours infilled by ripple cross-laminated sediment and/or clayey clasts occur frequently at the top of the deformed layers. The individual deformation events must have been separated by periods of erosion/accumulation in the lake. The erosional features are consistent with the frequent sharp and discordant top contacts of the SSDS layers (see Table 1), and show that the individual deformation processes occurred repetitively at contemporary surfaces (palaeosurfaces).

Mesoscale soft-sediment deformation structures

Injection structures

Description

The injection structures consist of sandy silt and silt. They have various sizes (from 0.2 to 40-cm high) and shapes (pipes to dykes) and commonly occur within all the deformed layers of unit 3 (Fig. 7). Most of the injection structures are confined within individual deformed layers (Fig. 7C and E), but some penetrate into the overlying sediments. For example, injections in layer SSDS-5 can be traced into and cutting through layer SSDS-6 as well as the overlying undeformed cross-laminated silty sand and fine sand, finally terminating in layer SSDS-7 (Fig. 7A and B). Some of the small-scale injections are filled with highly contorted finely laminated sandy silt.

There is a small grain size difference between the injected (sandy silt) and the host (silty sand) sediment, with the median diameter difference between 1.62 and 0.27 phi (Fig. 8A and B). In all cases, the injected sediment is somewhat finer-grained and less well sorted than the host sediment (Fig. 8B and C). The positive skewness (Sk) and cumulative grain-size distribution of both injected and host sediments show a high content of fines. Generally, the host sediments have a more positive skewness than the injected sediments.

Interpretation

The poorer sorting of the injected sediments can be explained by partial mixing with the surrounding sediments (Fig. 7C) or by the heterogeneity of the source sediment. In some layers with SSDS, the upper limit of the injections corresponds with the occurrence of cohesive clay laminae of low hydraulic conductivity (Fig. 7D). One factor apparently influencing the injection process is the thickness ratio between the mobilised and the host sediment within a single deformed layer.

The injection deformed the adjacent sediments leading to bending upward of laminae or layer boundaries as the result of passage of escaping water-sediment mix (Fig. 7B and E). The deformation geometry shows that fluid passage was mostly directly upward through the sediment succession. Additionally, mobilization of the sediment generated ball-and-pillow structures and caused fragmentation of more cohesive clay-rich laminae and the formation of load casts (Figs 6 and 7). The small-scale injections have penetrated into the overlying sand resulting in the upward deflection of the lamination within the sand beds to form an open to moderately tight upright anticlines (Fig. 7B). The injection feature shown in Fig. 7A likely fed a sand volcano on the former lake bed, later truncated by erosion. Alternatively, the vertical injection may have been connected with a subhorizontal sill indicating that the overlying sediment formed a cap trapping the escaping fluid-sediment mix. Both processes must have occurred relatively close to the contemporary bottom of the lake (at the surface or in the uppermost decimetres). The source of the injected sediment was in layer SSDS-5. The overlying sand of layer SSDS-6 possesses well developed load structures comprising dish-shaped synforms separated by tight, flame-like anticlines (Fig. 7B). These load structures are, in turn, cross cut by a sediment injection indicating that the whole sequence records several phases of deformation. The aforementioned features suggest elevated pore-water pressure and loss of sediment strength. Most indicative of pore-water pressure increase is the presence of two large-scale injection structures that start in layer SSDS-5 and cut through the overlying sediments (Fig. 7A and B). The upward bending of adjacent sediments as well as the occasionally observed internal fine-lamination inside the injection, clearly record an upward escape of the fluid driven by rapid pore-water pressure increase. The relative downward movement of SSDS-6 sediment documents a loading process that compensate the injection, while also in a liquefied state. Other examples are layers SSDS-1 and SSDS-10, where high pore-water pressure within thick silty deposits interbedded with a thin sandy layer caused the formation of large (in SSDS-1) and small (in SSDS-10) ball-and-pillow structures. In both cases, the grain size difference between the load structures and the surrounding injected sediments is noticeable.

Load casts and associated structures

Description

The style, complexity and deformation intensity of the load structures within the disrupted layers vary laterally across the exposed section (Figs 4, 5 and 6). In coarser-grained layers

SSDS-2 and SSDS-7 only load casts of similar sizes but various shapes and complex internal structures are observed, while within layers enriched in silt (SSDS-3 to -6 and SSDS-8 to -10) different types of load structures coexist. In the least deformed parts of the layers, open to moderate, upright to steeply inclined flat-bottomed synforms constituting load casts are often separated by narrow flame-like antiforms (Fig. 6A and G). In the more deformed parts of the layers, the necks of the structures become increasingly narrow forming more complex teardrop- to kidney-shaped structures (Fig. 8A). The deformed primary sedimentary structures (e.g. cross-lamination) are often preserved within the cores of the load casts. In the most deformed areas the originally laminated sediments are highly disrupted with the detached load casts forming isolated lighter coloured sand-balls or pillows contained within a contorted or homogenised matrix of darker brown sandy-silt matrix (Fig. 6D and H). In a plane view, the load structures together with the injections create a dense 3D network (Fig. 6H).

Three main groups of load casts are distinguished based on their shapes and internal structures: simple load casts, where internal lamination follows the regular outer shape of the load cast (type A) (Fig. 6A and B); complex load casts, where the internal lamination is contorted and there is no regular arrangement (type B) (Fig. 6D and G to H); and load casts with preserved, undeformed primary lamination (type C) (Fig. 6E). Among the detached load casts are pseudonodules, i.e. sand-balls of different shapes and sizes. Their sizes vary from few centimetres to decimetres. Small pseudonodules (with diameters not exceeding 2 cm) are present in the upper parts of layers SSDS-1 and SSDS-10, in layers SSDS-3, SSDS-4 and SSDS-8, while larger pseudonodules are irregularly distributed along the whole vertical and horizontal extent of layer SSDS-1 (Fig. 6D and F).

Interpretation

The formation of load structures is driven by Rayleigh-Taylor instability of two layers with different specific gravities (Allen, 1982a and references therein). According to Potter and Pettijohn (1977), the only requirement for the formation of such structures is accumulation of a bed of sand on a water-saturated deformable deposit. The A and B types of load casts developed due to sinking of sand (or sand interbedded with silt) into liquefied and/or fluidised sediments. The differences in the internal structures of type A and B load casts could result from the heterogeneity of the laminated deposits that sank (Fig. 6F and G). In contrast, type C load casts in the upper part of SSDS-1, with the non-deformed primary lamination must have developed in a single, rapid act of injection of the underlying sandy silt (cf. Pisarska-Jamroży *et al.*, 2018b, 2019a) leaving no visible evidence of loading (Pisarska-Jamroży *et al.*, 2019b). Thus, the sediment that the load casts consist of remains *in situ*, while only the surrounding sediment creeps upward ("pseudoloading" of Pisarska-Jamroży *et al.*, 2019b; Van Loon *et al.*, 2020). As the deformation proceeded, the originally laminated sediment became increasingly disrupted, with the synform-shaped load cast becoming progressively isolated and forming tear-drop to more complex rootless folds which gave rise to individual pseudonodules and sand-ball or pillow sets within a highly contorted to homogenised matrix. This silty sand matrix shows evidence of increasing liquefaction and mobilisation with the upward-oriented creep of fluidised sediment leading not only to the formation of injection features, but also to rotation and contortion of the pseudonodules and sand-balls or pillows.

The internal complexity of single load structures and their cross-cutting relationships with the injection structures within a single deformed layer indicate different phases of the lacustrine sediment loading without big time gaps in between (Figs 6D, H and 7A). The loading process might have generated single load casts, followed by drop-shaped load casts, flat-bottomed load casts and finally pseudonodules (Fig. 5).

Comparing the thicknesses and grain-size composition (Fig. 8) of all SSDS layers indicates that the sizes of load casts were controlled by the primary texture, thickness and structure of the deposits engaged in the deformation as well as possible lateral variations in pore-water pressure (e.g. SSDS-1 and -3 with similar grain size distribution but different ranges of individual SSDS sizes).

Broken-up sediment laminae

Description

Sets of detached silty sand laminae occur within host sandy silt sediment in layers SSDS-1 and SSDS-10 (Fig. 9). The thicknesses of the fragmented laminae do not exceed 5 mm, while the lengths range from 2 cm to 10 cm. The fragments of tabular dish-shaped broken-up laminae are either only slightly displaced, or chaotically distributed in the surrounding sediment. Some of them have roll-up shapes.

Interpretation

The fragmented laminae resulted from injection of liquefied sediment that caused lateral extension and tearing. The curved or rolled shapes of the laminae may reflect the softness of the surrounding sandy silt during deformation, and the extent of lateral advection.

Faults and joints from a younger phase of deformation

Description

Set of several dozens of faults and joints occur in the upper part of unit 3 (Figs 2B and 10). The high-angle, normal faults and joints cut and displace layers SSDS-8, -9 and -10 as well as the intervening sediments that show no evidence of deformation. Locally, also layer SSDS-7 is affected (Fig. 10A to C). The throws of normal faults vary between 0.5 cm and 8 cm. Some of the fractures show no displacement. Two main sets of faults and joints occur, with planes striking WSW-ENE and WNW-ESE, and dipping to NNE and SSE, respectively. The dip angles vary between 32° and 88° with the vast majority clustered between 50° and 85° (Fig. 10A'). The dihedral angle between the mean orientations of planes of each of the two main sets is 37° and the inferred direction of the principal stress ($\sigma 1$) is steeply inclined to subvertical (258°/75°).

In the central part of the outcrop, within the SSDS-8 sediments, seven angular trapezoid-shaped clasts consisting of plastically deformed sand and sandy silt are observed (Fig. 10C, D). The biggest, lowermost clast is at least 15x12 cm large (Fig. 10C) whereas the remaining six clasts are up to 4x4 cm or 5x2 cm. The shapes of these clasts are related to the faults and joints that cut the whole unit 3 (Fig. 10A). All of these clasts are surrounded by mixed massive or deformed silty and sandy matrix that does not belong to any of the lithofacies described above. The clasts, together with the surrounding sediment fill a steep, 20-cm-deep channel eroded in the lacustrine deposits (Fig. 10C and D).

Interpretation

The faults are classified as steeply inclined sets of conjugate hybrid faults. The failure surfaces were initiated at the transition from tensile to shear failure (cf. Hancock, 1985; Ramsey & Chester, 2004). Therefore, the jointing and faulting must have been initiated under sediment extension, likely due to ice-sheet loading during the Late Weichselian advance, when joints propagated parallel to the $\sigma 1$ direction, followed by an increasing impact of shearing.

The angular clasts most probably result from sediment slumping into the channel accompanied by disintegration. The preservation of primary structures in the clasts as well as their shapes suggests that this occurred in a frozen state. This event postdates the ductile deformation within all SSDS layers and may have been associated with the small-scale faulting and jointing mentioned above.

Microstructure analysis of SSDS

Four undisturbed oriented samples from layers SSDS-1, -3 and -10 were analysed in microscale to examine the complexity of SSDS and to constrain the factors controlling the style of deformation and the relationships between the individual structures. The samples were collected along a vertical profile though the exposed sediment with focus on small-scale and complex SSDS. Two samples came from SSDS-1 (Di1A, bottom and Di1B, top), one from SSDS-3 (Di3 spanning the whole vertical extent of the layer), and one from SSDS-10 (Di10).

Sample Di1A

The highly deformed and disrupted sediment in thin section Di1A is dissected by a single, steeply inclined, SW-dipping injection that cuts though the central part of the sample (Fig. 11A). The injection feature is crudely funnel-shaped widening upwards where it connects with an irregular area of massive sandy silt extending into the core of a folded and detached load cast (Fig. 11A). The injected sediment is internally laminated whereby a thin, outer layer of clay and/or silty clay coats the walls of the injection and its central part consists of pale-brown sandy silt. A weakly developed/preserved lamination within the sandy silt oriented parallel to its walls occurs locally. At its upper right end this lamination is folded within the core of the adjacent load cast (Fig. 11A), possibly indicating that the folding continued after the injection had ceased. A number of steeply inclined, small-scale (displacement c. 4 mm) faults occur in the highly deformed sediment immediately adjacent to the injection feature. These faults run parallel to the margins of the injection (Figs 11A and 13D), suggesting that brittle faulting may have occurred during the injection of fluidised sediment.

The laminated silt, sandy silt and silty sand in the lower part of the thin section are highly deformed with the primary sedimentary lamination locally disturbed by recumbent folds and subhorizontal shears (Fig. 11A). The lamination is clearly cross-cut and locally deflected upwards by the injection feature indicating that this feature post-dates deformation in this part of the thin section. In contrast, in the upper part of the thin section the sediment is disrupted by an upright to steeply inclined fold (Fig. 11A), which is part of a detached load cast.

Sample Di1B

This thin section (Fig. 11B) is dominated by a single, up to 4-cm wide, pipe-shaped injection of sandy silt surrounded by deformed and mixed sand and silt in the central part of the sample. The width of the injection decreases towards NE. The injection is weakly laminated, but to the SE the lamination is disturbed by a number of recumbent to gently inclined, very tight to isoclinal folds that possibly developed in response to the injection-induced folding. Above the injection structure, massive to very weakly bedded sand with sandy/silty intercalations that constitute a simple load cast contains rounded to irregular clayey intraclasts (Fig. 11B). These intraclasts are surrounded by coatings of sand grains (Fig. 13B) and may represent relicts of clay layers eroded during the deposition of sand. In the SW part of the sample, there are small-scale complex load casts with strongly deformed internal lamination cut and displaced by small injections. The mixed sediments in both upper and lower part of the section are locally cut by low-angle faults with displacements reaching 0.2 cm.

The evolution of the deformed samples Di1A and Di1B revealed by cross-cutting relationships suggests that several stages of deformation occurred in layer SSDS-1. Although distinct deformation successions are recorded in the cross-cutting relationships, the stages of deformation do not represent separate, individual events. Rather, the complex deformation observed in these samples is consistent with the deformation phases recording the folding and faulting of the sediments in layer SSDS-1 during a single, progressive deformation event. In both samples sandy silt injections cross-cut strongly folded and faulted sediments. This suggests that the mobilised sandy silt was injected into the already deformed and disrupted sediments and that liquefaction and advection of the injected sediment occurred in response to pore-water pressure increase caused by deformation. Small faults associated with the injection structures occur up to the margins of the injections, cutting through homogenised sand (Di1A; Fig. 11A). Thus, the injection was accompanied by faulting possibly resulting from volume changes caused by the movement of the fluidised sediment coupled with hydrofracturing generated by pore-water pressure increase. Extensional movements on these faults would have facilitated injection of the fluidised sediment by creating the required accommodation space. Subsequently, volume changes caused by injection of the fluidised sediment is thought to have caused folding and disruption of the overlying sediments resulting in the formation of load casts. The internal structure of the load casts clearly indicate that their formation is a complex process involving several stages leading to refolding of older folds near the bases of these detached, rootless synclines (Fig. 11A). The disharmonic, complex nature of these refolded structures is consistent with the elevated pore-water pressure at the time of deformation. High water pressure is also suggested by the diffuse nature of the lamination within the sand in the load cast at the top of sample Di1B (Fig. 11B). Pressurisation of pore water trapped in the intergranular spaces during folding could potentially lead to localised liquefaction of the sand and partial disruption of the lamination. Consequently, the complexity of the microstructural relationships and the wide range of deformation microstructures observed in samples Di1A and Di1B (Fig. 11) shows that even a single mesoscale event of soft-sediment deformation may comprise multiple sub-phases of ductile and brittle deformation accompanied by localised liquefaction, remobilisation and injection of the fluidised sediment.

Sample Di3

The central part of sample Di3 is dominated by two open synclines deforming weakly laminated sand and silty sand, and creating partially detached load casts separated by a 1-cm wide and up to 2-cm high cone-shaped injection structure (Fig. 12A). This sandy part of the sediment succession is covered by a massive to slightly mottled sandy silt whereby the contact zone between these deposits is highly complex, diffuse and irregular (Fig. 12A). The mottled sandy silt is apparently fed by the injection. This relationship, coupled with the complexity of the contact zone is consistent with the mottled sandy silt having been liquefied, mobilised and injected into its present position.

The sand in the central upper part of the thin section is underlain by thinly bedded to laminated sand, silt and clay that are dissected by numerous thin, pillar-shape vertical to subvertical small-scale injections (up to 2 mm wide) (Figs 12A and 13E). In the lowermost part of the thin section, a complex network of thin irregular sand-filled veinlets propagates both upwards and downwards from a much thicker sand layer (Fig. 12A). Injection of these sand-filled veinlets has resulted in the fragmentation of the underlying and overlying clay laminae into a series of tabular blocks (Fig. 13A, C). Although typically angular, some of these clay blocks show incipient rounding at the margins (Fig. 13A and C), possibly as a result of abrasion caused by the flow of fluidised sand. The sand-filled veinlets injected upward from the sand layer and dissecting the overlying clay laminae clearly terminate at the base of the overlying undeformed ripple-cross laminated sand (Fig. 13E). In the uppermost part of the thin section, several similar small-scale sand-filled veinlets connected to a 5-mm-thick silty sand layer are injected upward into a clay layer, which they dissect (Fig. 12A).

Three levels of deformation features occur within sample Di-3. All of these levels are sandwiched between layers or laminae of low-permeability clay that acted as barriers for vertical flow of pore water. Although liquefied, the primary lamination remained partly undeformed in the top and bottom levels of deformation. The occurrence of downward-oriented sand-filled veinlets in the lowermost part of the sample suggests that pore-water pressure rapidly increased within this level. This shows that soft-sediment deformation may not affect the entire sediment unit to the same extent and its intensity is controlled by the rheological properties of the sediment most likely resulting from the variations in grain sizes. We interpret all SSDS in sample Di3 as having formed during a single progressive deformation event not interrupted by any significant breaks and sediment stabilization.

Sample Di10

Sample Di10 was taken from the uppermost deformed layer and for the ease of description the thin section is divided into three parts (Fig. 12B). The bedding surfaces separating these three parts dip at an apparent angle of 20° towards SW (Fig. 12B), which is a unique feature among all analysed SSDS where bedding within the bounding undisturbed sediments is typically horizontal. The lower part of the thin section comprises a layer of sandy silt in which the primary sedimentary lamination is deformed/contorted and locally overprinted by liquefaction. In contrast, in the middle part of the thin section, primary planar bedding is undisturbed within a 2 to 3 cm thick layer of sandy silt and silty sand (Fig. 12B). The zone between the lower and the middle parts hosts several small pillar-shaped injections oriented upward that locally disturb the primary bedding of the middle part. The boundary between the middle and upper parts of the thin section is marked by a thin (up to 2 mm) clay lamina which is locally fragmented with tabular to slab-shaped pieces detached and incorporated into the overlying massive silty sand (Fig. 12B).

The upper part of the thin section comprises a 5-cm thick layer of massive sandy silt showing in places a weak, diffuse lamination and isolated rounded, elongate to irregular small (diameters 0.1-1 cm) pseudonodules (sand-balls) composed of massive to very weakly laminated sand (Fig. 12B). Some of the pseudonodules are enclosed by thin clay coatings. The locally preserved lamination within the pseudonodules is deformed suggesting that they are relicts of detached rootless folds. Elongate, thin to wispy tails composed of fine sand indicate that the pseudonodules rotated to some degree during deformation. This rotational movement may have accompanied the partial fluidisation and homogenisation of the host silty sand.

DISCUSSION

Liquefaction results from a sudden loss of shear strength of water-saturated porous granular sediment due to the loss of intergranular contacts when grain weight is temporarily transferred to the pore fluid (Allen, 1982a; Owen & Moretti, 2011). The characteristics of the ten sediment layers at Dyburiai section containing SSDS indicate that these layers experienced internal deformation related to sediment liquefaction, advection, and injection (cf. Owen & Moretti, 2011). These characteristics are: (1) the broad range of SSDS occurring exclusively within a narrow zone of the most liquefaction-prone sediments such as silty sand and sandy silt (Fig. 8) with the rather small grain-size differences between the loaded and injected sediments (Fig. 8) (Obermeier, 1996, 2009); (2) the abundance of injection structures and hydrofractures in micro- and mesoscale (Counts & Obermeier, 2012); (3) the distribution of SSDS along continuous sediment layers, often limited above and below by deposits of low hydraulic conductivity; and (4) the microstructures lacking any preferred orientation or distribution and showing overprinting of different processes over a short period of time, which suggests a “wet deformation process” (Menzies & Taylor, 2003).

Possible triggers of liquefaction-induced soft sediment deformation

Liquefaction can be triggered by various processes (Allen, 2003; Owen & Moretti, 2011) and in the following we consider several relevant possibilities.

Rapid aggradation of sediments

This trigger of deformation is linked to recurrent overloading by rapidly accumulating sediment, in particular as an effect of a non-uniform confining loading by ripple-cross laminated sand (Dżułyński & Kotlarczyk, 1962; Allen, 1982b). This process could have formed the load casts and injections, especially in the uppermost part of SSDS-1. However, the changing style of deformation, numerous injection structures, vertical repetition of layers with SSDS and lack of sedimentary structures indicative of rapid deposition (e.g. climbing ripples) make this mechanism unlikely as the main cause of deformation at Dyburiai section.

Periglacial processes, active layer deformation or cryoturbations

The study area was exposed to periglacial conditions during the Late Pleistocene (Baltrūnas *et al.*, 2007). Our OSL ages indicate that the lacustrine succession was deposited during the Lower Nemunas periglacial period of MIS 5d (Guobytė & Satkūnas, 2011; Gibbard & Lewin, 2016) when permafrost occurred in Lithuania (Baltrūnas *et al.*, 2007).

SSDS similar to those described here can develop under either periglacial conditions or in response to deep seasonal freezing of the ground leading to cryoturbation in the absence of permafrost (Van Loon, 2009; Vandenberghe, 2013) such as observed e.g. in Poland (Krzyszkowski, 1990; Kasse *et al.*, 1998). Several findings would be consistent with a periglacial origin of the deformations at Dyburiai, although this would require recurrent lake drainage or its complete freezing to the bottom.

Firstly, the periglacial activity or seasonal ground freezing can lead to laterally highly variable styles and intensities of deformation, such as at Dyburiai (Fig. 2B). The series of repetitive, generally regular, symmetrical, intensely folded structures observed within SSDS layers 3, 4, 5 and 6 (Figs 4 and 6) resemble type 3 structures in the classification of Vandenberghe (2013), and the soft-sediment deformation features in layers SSDS-7, -9 and -10 (Fig. 8A and B) and SSDS-8 (Fig. 4B) resemble type 4 and type 6 structures, respectively. Secondly, according to Vandenberghe (2013) formation of cryoturbations requires a reversed density gradient within the deforming medium, with folding and involution accompanied by liquefaction of the lower layer─this process may have occurred in the study area. Such conditions may occur beneath the permafrost layer due to poor water drainage, which at Dyburiai may have been caused by abundant clay interlayers. In any case, cryoturbation requires temporary and cyclic lake drainage, or freezing of the entire water column in the lake. However, there is no evidence of either of these scenarios in the study area. Thirdly, the sediment succession at Dyburiai contains multiple layers with SSDS, potentially indicative of repeated phases of deformation under periglacial conditions. Deformations in layers SSDS-7, 8 and 9 (Fig. 4A and B) are similar to the structures generated during the scaled centrifuge modelling experiments of thawing ice-rich silty and clayey soils overlain by sand conducted by Harris *et al*. (2000). Deformation within these layers could have occurred as a result of loading, cryohydrostatic injection and cryostatic heave (French, 2007; Vandenberghe, 2013). Cryohydrostatic injection may develop along narrow fissures and also as wider intrusions, but because of the deformation the original cracks and fissures are generally lost (Kasse, 1993; Vandenberghe, 2013), contrary to what we document at Dyburiai. Finally, all of SSDS layers were deformed at or close to the contemporary ground surface prior to or soon after burial, i.e., where the periglacial processes were most likely to occur.

Nevertheless, at the Dyburiai site the structures typical for periglacial conditions (cf. Van Vliet-Lanoë *et al.*, 2004; Van Loon *et al.*, 2020) are lacking. There are no thermal contraction cracks, wedge-shape structures (patterned ground, ice-wedge pseudomorphs) or lenticular/microlenticular cryostructures, which result from ice segregation in the sediment (e.g. French & Shur, 2010). Also, some features that are very unlikely to develop in periglacial conditions are commonly observed at Dyburiai: SSDS are confined to continuous, laterally extensive sediment layers and the shapes of most of the load structures are non-isometric and asymmetric (e.g. SSDS-1, Fig. 6D). To our knowledge, vertical succession of multiple layers with SSDS separated by erosion and accumulation events has never been ascribed to cryoturbations.

Glaciotectonic deformation

Soft-sediment deformation may result from proglacial and/or subglacial processes caused by ice-sheet masses moving over unconsolidated sediment (e.g. Hart & Boulton, 1991; Andersen *et al.*, 2005; Aber & Ber 2007; Van Loon, 2009 and references therein; Pedersen, 2014; Phillips *et al.,* 2018; Pisarska-Jamroży *et al.*, 2018b). However, at Dyburiai site there is no till directly overlying the layers with deformations, there are no typical glaciotectonic features such as low-angle thrust faults, recumbent folds or shear zones, and there is no consistent orientation of the deformation structures that would otherwise indicate sediment displacement due to unidirectional glacier stress. The layers with SSDS are only deformed internally, while their tops and bottoms are undisturbed. Also, the sediments immediately below and above the layers with deformations are undisturbed. Finally, the time-frame of deposition and deformation combined with the regional stratigraphy is inconsistent with multiple ice advances and retreats needed to generate the pattern of deformation in question. We also note the absence of dumpstones and dropstones, which would otherwise suggest a possible liquefaction induced by large iceberg calving events (cf. Phillips *et al.*, 2018).

Mass flows

Gravity mass transport may be ruled out due to the lack of slump folds or shear zones and absence of any mass flows deposits. The sediment architecture consisting of internally deformed layers bounded by undeformed deposits is very distinct whereas mass transport deposits would be chaotically mixed or massive. There are no consistent dip directions or slope angles. Moreover, according to Allen (1982b) the occurrence of regularly- distributed pseudonodules and ball-and-pillow structures widespread across the whole section is inconsistent with sediment affected by mass flow processes.

Seismic activity

Cyclic stresses induced by the passage of seismic waves lead to increase in pore-water pressure (Owen & Moretti, 2011). Soft sediments can then experience seismicity-induced liquefaction as a secondary, off-fault earthquake effect generating seismites, i.e. layers with SSDS of seismic origin (Wheeler, 2002; Obermeier, 2009; Reicherter *et al.*, 2009 and references therein; Sims, 2012). The threshold magnitude of an earthquake for sediment liquefaction is estimated as 4.5 (Ambraseys, 1988; Marco & Agnon, 1995). However, it is believed that water-saturated sediments can experience liquefaction at much lower local magnitudes and may remain instable during the subsequent aftershocks of smaller intensity (Phillips *et al.*, 2018 and references therein).

Several lines of evidence support the seismicity-induced origin of the SSDS at Dyburiai. Firstly, the repeated deformed layers correspond to “superposed deformation beds” of Gibert *et al*. (2011) considered a key characteristic of palaeoseismites (cf. Hilbert-Wolf *et* *al.*, 2009 and references therein; Owen & Moretti, 2011). Owen & Moretti (2011) state that deformation beds mobilized by seismically induced liquefaction appear repeatedly through a vertical succession of soft sediment. This criterion has been widely used to identify events of seismite formation in various tectonic settings in both consolidated and unconsolidated rocks (e.g. Sims, 1975; Hibsch *et al.*, 1997; Hilbert-Wolf *et al.*, 2009, 2016; Gibert *et al.*, 2011; Alsop & Marco, 2011; Alsop *et al.,* 2019; Mazumder *et al.*, 2016; Van Loon *et al.*, 2016; Pisarska-Jamroży *et al.*, 2018a; Morsilli *et al.*, 2020). Consistent with the seismic origin is that the individual deformed layers at Dyburiai are laterally extensive and have well-defined tops and bottoms (e.g. SSDS-3, -4, -5, -6, -7 and -8; c.f. Van Loon *et al.*, 2016; Pisarska-Jamroży *et al.*, 2019a), which may be interpreted as an indication of tranquillity phases between the seismic events (see below). In our interpretation, the injection features associated with the SSDS suggest that liquefaction occurred in response to a sudden and strong increase in pore-water pressure, similar to small-scale features associated with palaeoseismic activity elsewhere (Counts & Obermeier, 2012).

Other characteristics that are consistent with the seismic origin are (1) a reversed gravity gradient of deformed and host sediments (injection of SSDS-5 sediments into SSDS-7 and internal deformation of SSDS-7; Figs. 5, 8A, B; cf. Moretti *et al.*, 1999) and (2) wide structural variety of SSDS (e.g. load structures, injections, broken-up laminae) (cf. Sims, 2012), all corresponding to the characteristics imposed by known (c.f. Lunina *et al.*, 2012; Giona Bucci *et al.*, 2019) or presumed earthquakes (cf. Hibsch *et al.*, 1997; Menzies & Taylor, 2003; Mugnier *et al.*, 2011).

Being located in the south-western part of the East European Craton, the study area was previously considered as a seismically inactive, stable continental core region. However, two M=5 and M=5.2 earthquakes occurred in 2004, with epicentre on the Sambia Peninsula (Kaliningrad District of Russia) and shallow hypocentre at a depth of 16–20 km (Gregersen *et* *al.*, 2007; Fig. 14). The earthquake was triggered by right-lateral strike slip on a WNW-ESE oriented near-vertical fault parallel to the Tornqiust-Teisseyre zone, and it caused moderate damage at relatively large distances, e.g. in NE Poland and W Lithuania (Gregersen *et al.*, 2007; Fig. 14). Some lower-magnitude seismic activities have been recorded since 2004 and past earthquakes are now interpreted from instrumental and historical records (Pačėsa & Šliaupa, 2011; Lazauskienė *et al.*, 2012; Nikulins, 2017; Nikulins & Assinovskaya, 2018; Fig. 14). The recently recorded earthquakes include the 1988 event with an estimated magnitude of 2–3 and epicentre in Latvia in close proximity to Dyburiai (Lazauskienė *et al.*, 2012; Nikulins & Assinovskaya, 2018), and the 2015 event with epicentre close to the Curonian Lagoon (SE Baltic Sea) with magnitude 2.6 and hypocentre at the depth of just 1.0 km (Nikulins & Assinovskaya, 2018). Both of these earthquakes are connected to pre-Quaternary faults in bedrock. The W-E striking Telšiai fault zone is the most prominent tectonic structure in the proximity of the study area (Pačėsa & Šliaupa, 2011; Lazauskienė *et al*., 2012; Fig. 14). This fault zone, plunging to the north with high angle (60-80°), was established during late Silurian – early Devonian NW-SE directed compression related to the collision of Laurentia and Baltica (Šliaupa, 2002). Afterwards it was reactivated several times in transpressional regime (Šliaupa, 2002). The likely mechanism of the possible neotectonic reactivation of these faults is glacioisostatic adjustment (GIA, cf. Johnston, 1987; Muir-Wood, 2000; Stewart *et al.*, 2000; Grollimund & Zoback, 2001; Steffen *et al.*, 2014; Brandes *et al.*, 2015, 2018) due to stress fluctuations caused by waxing and waning ice sheets. Modelling of Coulomb Failure Stress change (δCFS) during the last 120,000 years supports a glacially-induced fault reactivation in the study area and suggests positive values of δCFS in the time span between 120-70 ka, 50-45 ka, and 38-28 ka as well as from ca. 15.5 ka BP up to the present (Steffen et al., 2019). Our SSDS formed shortly after 119.7–91.1 ka, at the time when GIA was possible (Steffen *et al.*, 2019) and maybe induced by relaxation following the retreat of the Saalian ice sheet. However, numerical simulations have limitations imposed by tectonic and glaciological assumptions so that the positive δCFS periods vary between the models (Steffen *et al.*, 2019 and references therein). Other sites with Pleistocene or Holocene sediments interpreted as GIA-induced seismites have recently been documented in other north-eastern areas of the Peribalticum (Van Loon *et al.*, 2016; Druzhinina *et al.*, 2017; Pisarska-Jamroży *et al.*, 2019a; Woźniak *et al.*, 2019).

Still, it should be noted that some of the criteria used to identify seismites (Hilbert-Wolf *et al.*, 2009 and references therein; Owen & Moretti, 2011) are not met. Firstly, the vertical extent of the deformed layers is unknown due to the outcrop limitations and no documentation of other SSDS exists in the vicinity of the Dyburiai site, which restricts spatial inferences. Secondly, there are no accurate data of the fault acting as a possible source of seismic wave, so that the "zonation of complexity with distance from a fault" criterion is not applicable. In sum, our interpretation–although consistent with the original data presented above–should be scrutinized by independent future studies.

Palaeosurfaces with erosional features constrain the number of seismicity-induced liquefaction events

For years, there has been a discussion as to whether the number of seismites corresponds to the number of earthquakes (=seismic events) or multiple layers can be deformed during a single seismic event (e.g. Rossetti & Góes, 2000; Van Loon, 2009; Van Loon *et al*., 2016). Sediments undergo seismicity-induced liquefaction mainly close to the ground surface (Obermeier, 1996, 2009; Obermeier *et al.*, 2002 and references therein; Van Loon *et al*., 2020) and the depth of liquefaction is limited by an increasing overburden load and thus shear strength of sediment (Obermeier *et al.*, 2002). Our results, with particular reference to the erosional tops of the layers with SSDS, are useful to decipher the number of seismic events that caused repetitive sediment liquefaction. In the uppermost parts of at least seven layers with SSDS numerous erosional features (scours infilled by ripple cross-laminated sediment and/or relicts of clay layers (Figs. 3B, 4, 6, 7, 11B)) occur. Moreover, the presence of truncated injections or/and sand volcanoes on the former lake bed was suggested (Fig. 7A, B). Considering the relatively slow rate of deposition (i.e. rhythmical deposition from low-energy lacustrine environment dominated by deposition from slowly flowing water and deposition from currents, and lack of sediments typical for rapid aggradation) and the presence of at least seven erosional surfaces, we conclude that the sediment must have repetitively undergone liquefaction followed by deformation at (or very close to) the contemporary lake bed. Thus, at least seven separate seismic events might have affected the sedimentary succession at Dyburiai study site. This suggestion corresponds with the observations of Van Loon *et al.* (2016), but oposes to Gibert *et al.* (2011) who interpreted multiple deformed layers as an outcome of a single shaking event.

In most cases, a single layer of silty sediment was initially mobilized and then its injection caused deformation of sand. The subsequent liquefaction events could have affected also the deeper parts of the sedimentary succession (up to 1 m of depth), as recorded in layers SSDS-5 to SSDS-7 where the injected sediment cut through the overlying sediment an likely formed a sand volcano at the top of SSDS-7 (Fig. 7A, B). At the same time, the already deformed layers SSDS-1 to SSDS-4 were not affected by the liquefaction again. This suggests that in such multi-layered successions of sand interbedded with silt, a single liquefaction event is limited to the uppermost few decimetres.

CONCLUSIONS

The following conclusions can be drawn regarding the sediment record at the Dyburiai site:

1. The lacustrine part of the succession deposited during MIS 5d consists of ten individual layers hosting internal, liquefaction-induced SSDS interbedded with undeformed sediments.
2. The erosional features observed at the tops of multiple layers with SSDS (scours infilled with ripple-cross laminated sediment, clayey clasts as relicts of clay layers, truncated tops of injection structures and sandy volcanoes) show that the repetitive deformation phases were separated by periods of erosion, formation of new activation surfaces, and sediment deposition. Thus, the deformation events must have happened repetitively, at the contemporary lake beds (palaeosurfaces).
3. The most probable trigger of SSDS formation is seismic activity caused by fault reactivation possibly due to glacioisostatic adjustment following the retreat of the Scandinavian Ice Sheet after the Saalian glaciation. Accordingly, at least seven recurrent earthquakes separated by periods of tectonic tranquillity, erosion and deposition are suggested.
4. Mesoscale brittle deformation (faulting, jointing) occurred at a later, at present unconstrained stage.
5. Clay laminae facilitated local pore-water pressure buildup and limited the water migration.
6. Single liquefaction processes affecting any layer with SSDS consisted of multiple deformation stages resulting in the formation of complex, typically ductile deformation microstructures.

This study emphasizes the possible impact of seismic activity on soft-sediment mobilization in areas affected by ice sheet loading during the Quaternary glaciations, including the intraplate regions currently classified as aseismic and/or areas of low-seismicity. The key criterion for our interpretation is the recognition of erosional top surfaces that limit the individual layers with SSDS. These erosional surfaces, indicating that deformation occurred at or very close to the contemporary lake bed (palaeosurface) can be broadly used to identify soft- sediment affected by liquefaction-related deformation, regardless of the actual trigger mechanism.

ACKNOWLEDGEMENTS

We would like to thank the participants of the International Palaeoseismological Field Workshop in 2018 in Lithuania and Latvia for fruitful discussions, Dr. A. Damušytė (LGT) for fieldwork assistance and P. Szymura (AMU) for conducting grain size analysis. The study has been financially supported by a grant allocated to the GREBAL project (No. 2015/19/B/ST10/00661) from the National Science Centre, Poland. The microstructural analysis part was supported by the Polish National Agency for International Exchange (NAWA) Iwanowska Programme (No. PPN/IWA/2018/1/00061/U/0001). Emrys Phillips publishes with permission of the Director of the British Geological Survey.

REFERENCES

Aber, J.S. and **Ber, A.** (2007) Glaciotectonism. Developments in Quaternary Science, Vol. 6. Elsevier, Amsterdam, 246 pp.

Allen, J.R.L. (1982a) Liquidization, liquidized sediment, and the sedimentation of dense particle dispersions. In: Allen, J.R.L., *Sedimentary Structures, Their Character and Physical Basis, Vol. 2.*, Elsevier, Amsterdam, 293-342.

Allen, J.R.L. (1982b) Soft-sediment deformation structures. In: Allen, J.R.L., *Sedimentary Structures, Their Character and Physical Basis, Vol. 2.*, Elsevier, Amsterdam, 343-394.

Allen, J.R.L. (2003) Load Structures. In: *Encyclopedia of sediments and sedimentary rocks* (Ed. G.V. Middleton), pp. 413-414. Kluwer Academic Publishers, Dordrecht.

Alsop, G.I. and **Marco, S.** (2011). Soft-sediment deformation within seismogenic slumps of the Dead Sea Basin. *Journal of Structural Geology*, **33**, 433-457.

Alsop, G.I., Weinberger, R., Marco, S. and **Levi, T.** (2019) Identifying soft-sediment deformation in rocks. *Journal of Structural Geology*, **125**, 248-255.

Ambraseys, N. (1988) Engineering seismology. *Earthquake Engineering and Structural Dynamics*, **17**, 1-105.

Andersen, L.T., Hansen, D.L. and **Huuse, M.** (2005) Numerical modelling of thrust structures in unconsolidated sediments: implications for glaciotectonic deformation. *Journal of Structural Geology*, **27**, 587-596.

Anketell, J.M., Cegła, J. and **Dżułyński, S.** (1969) Unconformable surfaces formed in the absence of current erosion. *Geologica Romana*, **8**, 41-46.

Anketell, J.M., Cegła, J. and **Dżułyński, S.** (1970) On the deformational structures in systems with reversed density gradient. Annales de la Societe Geologuique de Pologne, **40**, 3-30.

Baltrūnas, V., Švedas, K. and **Pukelytė, V.** (2007) Palaeogeography of South Lithuania during the last ice age. *Sedimentary Geology*, **193**, 221-231.

Bertran, P., Font, M., Giret, A., Manchuel, K. and **Sicilia, D.**, 2019. Experimental soft-sediment deformation caused by fluidization and intrusive ice melt in sand. *Sedimentology*, **66**, 1102-1117.

Brandes, C. and **Winsemann, J.** (2013) Soft-sediment deformation structures in NW Germany caused by Late Pleistocene seismicity. *International Journal of Earth Sciences*, **102**, 2255-2274.

Brandes, C., Steffen, H., Steffen, R., and **Wu, P.** (2015) Intraplate seismicity in northern Central Europe is induced by the last glaciation. *Geology*, **43**, 611-614.

Brandes, C., Steffen, H., Sandersen, P.B.E., Wu., P. and **Winsemann, J.** (2018) Glacially induced faulting along the NW segment of the Sorgenfrei-Tornquist Zone, northern Denmark: Implications for neotectonics and Lateglacial fault-bound basin formation. *Quaternary Science Reviews*, **189**, 149-168.

Brooks, G.R. (2018) Deglacial record of palaeoearthquakes interpreted from mass transport deposits at three lakes near Rouyn-Noranda, north-western Quebec, Canada. *Sedimentology*, **65**, 2439-2467.

Brooks, G.R. and **Adams, J.** (2020) A review of evidence of glacially-induced faulting and seismic shaking in eastern Canada. *Quaternary Science Reviews*, **228**, 106070. https://doi.org/10.1016/j.quascirev.2019.106070.

Counts, R. and **Obermeier, S.F.** (2012) Seismic signatures: Small-scale features and ground fractures. In: *Recent Advances in North American Paleoseismology and Neotectonics East of the Rockies* (Eds R.T. Cox, M.P. Tuttle, O.S. Boyd and J. Locat), *Geological Society of America Special Paper*, 493, 203-219

Druzhinina, O., Bitinas, A., Molodkov, A. and **Kolesnik, T.** (2017) Palaeoseismic deformations in the Eastern Baltic region (Kaliningrad District of Russia). *Estonian Journal of Earth Sciences*, **66**, 119-129.

Dżułyński, S. and **Kotlarczyk, J.** (1962) On load-casted ripples. *Annales Societetis Geologorum Poloniae*, **32**, 147-160.

Folk, R.L. and **Ward, W.C.** (1957) Brazos River bar: a study in the significance of grain size parameters. *Journal of Sedimentary Petrology*, **27**, 3-26.

French, H.M. and **Shur, Y.L.** (2010). The principles of cryostratigraphy. *Earth-Science Reviews*, **101**, 190-206.

Gibbard, P.L. and **Lewin, J.**, 2016. Partitioning the Quaternary. *Quaternary Science Reviews* **151**, 127-139.

Gibert, L., Alfaro, P., García-Tortosa, F.J. and **Scott, G.** (2011). Superposed deformed beds produced by single earthquakes (Tecopa Basin, California): Insights into paleoseismology. *Sedimentary Geology*, **235**, 148-159.

Giona Bucci, M., Smith, C.M., Almond, P.C., Villamor, P. and **Tuttle, M.P.** (2019). Micromorphological analysis of liquefaction features in alluvial and coastal environments of Christchurch, New Zealand. *Sedimentology, 66*, 963-982.

Gregersen, S., Wiejacz, P., Dębski, W., Domański, B., Assinovskaya, B., Guterch, B., Mäntyniemi, P., Nikulins, V.G., Pačėsa, A., Puura, V., Aronov, A.G., Aronova, T.I., Grünthal, G., Husebye, E.S. and **Šliaupa, S.** (2007). The exceptional earthquakes in Kaliningrad district, Russia on September 21, 2004. *Physics of the Earth and Planetary Interiors*, **164**, 63-74.

Grollimund, B. and **Zoback, M.D.** (2001). Did deglaciation trigger intraplate seismicity in the New Madrid seismic zone? *Geology*, **29**, 175-178.

Grube, A. (2019) Palaeoseismic structures in Quaternary sediments, related to an assumed fault zone north of the Permian Peissen-Gnutz salt structure (NW Germany) – Neotectonic activity and earthquakes from the Saalian to the Holocene. *Geomorphology*, **328**, 15-27.

Guobytė, R. (2000). Revision of geomorphological map at a scale of 1:200 000. Lithuanian Geological Survey, Vilnius. (In Lithuanian; manuscript in the archive of Lithuanian Geological Survey).

Guobytė, R. and **Satkūnas, J.** (2011). Pleistocene Glaciations in Lithuania. In: *Quaternary Glaciations – Extent and Chronology: A Closer Look* (Eds. J. Ehlers, P.L. Gibbard and P.D. Hughes), pp. 231-246. Elsevier, Amsterdam.

Hancock, P.L. (1985) Brittle microtectonics: principles and practice. *Journal of Structural Geology*, **7**, 437-457.

Harms, J.C., Southard, J.B. and **Walker, R.G.** (1982) Structures and sequences in clastic rocks. Short Course No. 9 Lecture Notes. SEPM, Tulsa, 459 pp.

Harris, C., Murton, J. and **Davies, M.C.** (2000) Soft-sediment deformation during thawing of ice-rich frozen soils: results of scaled centrifuge modelling experiments. *Sedimentology*. **47**, 687-700.

Hart, J.K. and **Boulton, G.S.** (1991) The interrelation of glaciotectonic and glaciodepositional processes within the glacial environment. *Quaternary Science Reviews* **10**, 335-350.

Hibsch, C., Alvarado, A., Yepes, H., Perez V.H. and **Sébrier, M.** (1997) Holocene liquefaction and soft-sediment deformation in Quito (Ecuador): A paleoseismic history recorded in lacustrine sediments. *Journal of Geodynamics* **24**, 259-280.

Hilbert-Wolf, H.L., Simpson, E.L., Simpson, W.S., Tindall, S.E. and **Wizevich, M.C.** (2009) Insights into syndepositional fault movement in a foreland basin; trends in seismites of Upper Cretaceous Wahweap Formation, Kaiparowits Basin, Utah, USA. *Basin Research*, **21**, 856-871.

Hilbert-Wolf, H.L., Roberts, E.M. and **Simpson, E.L.** (2016) New sedimentary structures in seismites from SW Tanzania: Evaluating gas- vs. water-escape mechanisms of soft-sediment deformation. *Sedimentary Geology*, **344**, 253-262.

Horváth, Z., Michéli, E., Mindszenty, A. and **Berényi-Üvegesc, J.** (2005) Soft-sediment deformation structures in Late Miocene–Pleistocene sediments on the pediment of the Mátra Hills (Visonta, Atkár, Verseg): Cryoturbation, load structures or seismites? *Tectonophysics* **410**, 81-95.

Johnston, A.C. (1987) Suppression of earthquakes by large continental ice sheets. *Nature*, **330**, 467-469.

Jusienė, A. (2012) Spatial geological mapping at a scale of 1:50 000 in the Plateliai area. Lithuanian Geological Survey, Vilnius. (In Lithuanian; manuscript in the archive of Lithuanian Geological Survey).

Kasse, C. (1993) Periglacial environments and climatic development during the Early Pleistocene Tiglian stage (Beerse Member) in northern Belgium. *Geologie en Mijnbouw*, **72**, 107-123.

Kasse, C., Huijzer, A.S., Krzyszkowski, D., Bohncke, S.J.P. and **Coope, G.R.** (1998) Weichselian Late Pleniglacial and Late-glacial depositional environments, Coleoptera and periglacial climatic records from central Poland (Bełchatów). *Journal of Quaternary Science*, **13**, 455-469.

Krzyszkowski, D., 1990. Middle and Late Weichselian stratigraphy and palaeoenvironments in central Poland. *Boreas* **19**, 333-350.

Lazauskienė, J., Pačėsa, A. and **Satkūnas, J.** (2012). Seismotectonic and seismic hazard maps of Lithuania – recent implications of intracratonic seismicity in the Eastern Baltic Region. *Geologija*, **54**, 1-9.

Lunina, O.V, Andreev, A.V. and **Gladkov, A.S.** (2012) The Tsagan earthquake of 1862 on Lake Baikal revisited: a study of secondary coseismic soft-sediment deformation. **Russian Geology and Geophysics,** *53*, 594-610.

Mahaney, W.C., Dirszowsky, R.W., Milner, M.W., Menzies, J., Stewart, A., Kalm, V., and **Bezada, M.** (2004) Quartz microtextures and microstructures owing to deformation of glaciolacustrine sediments in the northern Venezuelan Andes. *Journal of Quaternary Science*, **19**, 22-33.

Marco, S. and **Agnon, A.** (1995) High-resolution stratigraphy reveals repeated earthquake faulting in the Masada Fault Zone, Dead Sea Transform. *Tectonophysics*, **408**, 101-112.

Mazumder, R., Van Loon, A.J., Malviya, V.P., Arima M. and **Ogawa Y.** (2016) Soft-sediment deformation structures in the Mio-Pliocene Misaki Formation within alternating deep-sea clays and volcanic ashes (Miura Peninsula, Japan). *Sedimentary Geology*, **344**, 323-335.

McKee, E.D., Crosby, E.J. and **Berryhill, H.L.** (1967) Flood deposits, Bijou Creek, Colorado. *Journal of Sedimentary Petrology*, **37**, 829-851.

Menzies, J. and **Taylor, J.M.** (2003). Seismically induced soft-sediment microstructures (seismites) from Meikleour, western Strathmore, Scotland. *Boreas*, **32**, 314-327.

Menzies, J. and **van der Meer, J.J.M.** (2018) Micromorphology and microsedimentology of glacial sediments, In: *Past Glacial Environments* (Eds J. Menzies and J.J.M van der Meer) 2nd edn, pp. 753-806. Elsevier, Amsterdam.

Miall, A.D. (1977) A review of braided river depositional environment. *Earth Science Reviews,* **13**, 1-62.

Moretti, M. and **Van Loon, A.J.** (2014) Restrictions to the application of 'diagnostic' criteria for recognizing ancient seismites. *Journal of Palaeogeography*, **3**, 162-173.

Moretti, M., Alfaro, P., Caselles, O. and **Canas, J.A.** (1999) Modelling seismites with a digital shaking table. *Tectonophysics*, **304**, 369-383.

Morsilli, M., Giona Bucci, M., Gliozzi, E., Lisco, S. and **Moretti, M.** (2020) Sedimentary features influencing the occurrence and spatial variability of seismites (late Messinian, Gargano Promontory, southern Italy). *Sedimentary Geology*, *401*, 105628. https://doi.org/10.1016/j.sedgeo.2020.105628

Mugnier, J.L., Huyghe, P., Gajurel, A.P., Upreti, B.N. and **Jouanne, F.** (2011) Seismites in the Kathmandu basin and seismic hazard in central Himalaya. *Tectonophysics* **509**, 33-49,

Muir-Wood, R. (2000) Deglaciation seismotectonics: a principal influence on intraplate seismogenesis at high latitudes. *Quaternary Science Reviews*, **19**, 1399-1411.

Nikulins, V. (2017) Seismicity of the East Baltic region and application-oriented methods in the conditions of the low seismicity. Academic edition. University of Latvia, Riga, 291 pp.

Nikulins, V. and **Assinovskaya, B.** (2018) Seismicity of the East Baltic region after the Kaliningrad earthquakes on 21 September 2004. *Baltica* **31**, 35-48.

Obermeier, S.F. (1996) Use of liquefaction-induced features for paleoseismic analysis. An overview of how seismic liquefaction features can be distinguished from other features and how their regional distribution and properties of source sediment can be used to infer the location and strength of Holocene paleo-earthquakes. *Engineering Geology*, **44**, 1-76.

Obermeier, S.F. (2009) Using liquefaction-induced and other soft-sediment features for paleoseismic analysis. In: *Paleoseismology* (Ed. J.P. McCalpin) 2edn, pp. 487-564. Elsevier, New York.

Obermeier, S.F., Pond, E.C., Olson, S.M. and **Green, R.A.** (2002) Paleoliquefaction studies in continental settings. In: *Ancient Seismites* (Eds. F.R. Ettensohn, N. Rast and C.E. Brett), *GSA Special Paper*, **359**, 13-27.

Owen, G. and **Moretti, M.** (2008) Determining the origin of soft-sediment deformation structures: a case study from Upper Carboniferous delta deposits in south-west Wales, UK. *Terra Nova*, **20**, 237-245

Owen, G. and **Moretti, M.** (2011) Identifying triggers for liquefaction-induced soft-sediment deformation in sands. *Sedimentary Geology*, **235**, 141-147.

Owen G., Moretti M. and **Alfaro P.** (2011) Recognising triggers for soft-sediment deformation: Current understanding and future directions. *Sedimentary Geology*, **235**, 133-140.

Pačėsa A. and **Šliaupa S.** (2011) Seismic activity and seismic catalogue of the East Baltic region. *Geologija*, **53**, 134-146.

Pedersen, S.A.S. (2014) Architecture of Glaciotectonic Complexes. *Geosciences* **4**, 269-296.

Phillips, E., Evans, D.J.A., van der Meer, J.J.M. and **Lee, J.R.** (2018) Microscale evidence of liquefaction and its potential triggers during soft-bed deformation within subglacial traction tills. *Quaternary Science Reviews* **181**, 123-143.

Pisarska-Jamroży, M. (2008) Zonation of glaciomarginal environment inferred from Pleistocene deposits of Myslibórz Lakeland, NW Poland. *Geografiska Annaler: Series A, Physical Geography*, **90**, 237-249

Pisarska-Jamroży, M. (2013) Varves and megavarves in the Eberswalde Valley (NE Germany) – a key for the interpretation of glaciolimnic processes. *Sedimentary Geology*, **291**, 84-96.

Pisarska-Jamroży, M. and **Zieliński, T.** (2014) Pleistocene sandur rhythms, cycles and megacycles: Interpretation of depositional scenarios and palaeoenvironmental conditions. *Boreas*, **43**, 330-348.

Pisarska-Jamroży, M., Belzyt, S., Börner, A., Hoffmann, G., Hüneke, H., Kenzler, M., Obst, K., Rother, H. and **Van Loon, A.J.** (2018a) Evidence from seismites for glacioisostatically induced crustal faulting in front of an advancing land-ice mass (Rügen Island, SW Baltic Sea). *Tectonophysics*, **745**, 338-348.

Pisarska-Jamroży, M., Belzyt, S., Bitinas, A., Jusienė, A., Damušytė, A. and **Woronko, B.** (2018b) A glaciolacustrine succession (Dyburiai outcrop, NW Lithuania) with numerous deformed layers sandwiched between undeformed layers. In: *Soft-sediment* *deformation structures and palaeoseismic phenomena in the South-eastern Baltic Region. Excursion guide of International Palaeoseismological Field Workshop* (Eds. M. Pisarska-Jamroży and A. Bitinas, A.), pp. 43-38. Lithuanian Geological Survey, Lithuanian Geological Society, Vilnius.

Pisarska-Jamroży, M. and **Woźniak, P.P.** (2019) Debris flow and glacioisostatic-induced soft-sediment deformation structures in a Pleistocene glaciolacustrine fan: The southern Baltic Sea coast, Poland. *Geomorphology*, **326**, 225-238.

Pisarska-Jamroży, M., Belzyt, S., Bitinas, A., Jusienė, A. and **Woronko, B.** (2019a) Seismic shocks, periglacial conditions and glacitectonics as causes of the deformation of a Pleistocene meandering river succession in central Lithuania. *Baltica*, **32**, 62-77.

Pisarska-Jamroży, M., Woronko, B., Bujak, Ł., Bitinas, A., Belzyt, S. and **Mleczak, M.** (2019b) Large-scale deformation structures characterize glaciolacustrine kame sediments—a new kame-investigation approach. *INQUA Congress 25–31.07.2019, Dublin, Ireland. Abstract book.* O-1128.

Potter, P.E. and **Pettijohn, F.J.** (1977) Paleocurrents and Basin Analysis. 2nd Edition. Springer-Verlag, New York, 425 pp.

Ramsey, J.M. and **Chester, F.M.** (2004) Hybrid fracture and the transition from extension fracture to shear fracture. *Nature*, **428**, 63-66.

Reicherter, K., Michetti, A.M. and **Silva, P.G.** Palaeoseismology: historical and prehistorical records of earthquake ground effects for seismic hazard assessment. In: *Palaeoseismology: Historical and Prehistorical Records of Earthquake Ground Effects for Seismic Hazard Assessment* (Eds. K. Reicherter, A.M. Michetti and P.G. Silva), *The Geological Society, London, Special Publications*, 316, 1-10.

Rossetti, D.F. and **Góes, A.M. (2000)** Deciphering the sedimentological imprint of paleoseismic events: an example from the Aptian Codó Formation, northern Brazil. *Sedimentary Geology*, **135**, 137–156.

Sims, J.D. (1975) Determining earthquake recurrence intervals from deformational structures in young lacustrine sediments. *Tectonophysics*, **29**, 141-152.

Sims, J.D. (2012) Earthquake-induced load casts, pseudonodules, ball-and-pillow structures, and convolute lamination: Additional deformation structures for paleoseismic studies. In: *Recent advances in North American paleoseismology and neotectonics East of the Rockies* (Eds. R.T. Cox, M.P. Tuttle, O.S. Boyd, J. Locat, J.), *Geological Society of America Special Paper*, 493, 191-201.

Šliaupa S. (2002) Kinematic features of the Telšiai fault in Western Lithuania: structural and permeability prognosis. *Geologja***, 32**, 24-30. [in Lithuanian with English summary and abstract]

Steffen, H., Steffen, R. and **Tarasov, L.** (2019) Modelling of glacially-induced stress changes in Latvia, Lithuania and the Kaliningrad District of Russia. *Baltica*, **32**, 78-90.

Steffen, R., Steffen, H., Wu, P. and **Eaton, D.W.** (2014) Stress and fault parameters affecting fault slip magnitude and activation time during a glacial cycle. *Tectonics*, **33**, 1461-1476.

Stewart, I.S., Sauber, J. and **Rose, J.** (2000) Glacio-seismotectonics: ice sheets, crustal deformation and seismicity. *Quaternary Science Reviews*, **19**, 1367-1389.

Towhata, I., Maruyama, S., Kasuda, K., Koseki, J., Wakamatsu, K., Kiku, H., Kiyota T., Yasuda, S., Taguchi, Y., Aoyama, S. and **Hayashida, T.** (2014) Liquefaction in the Kanto region during the 2011 off the pacific coast of Tohoku earthquake. *Soils and Foundations*, **54**, 859-873.

Vandenberghe, J. (2013) Cryoturbation Structures. In: *The Encyclopedia of Quaternary Science, vol. 3* (Ed. S.A. Elias), pp. 430-435. Elsevier, Amsterdam.

Van Loon, A.J. (2009) Soft-sediment deformation structures in siliciclastic sediments: an overview. *Geologos*, **15**, 3-55.

Van Loon, A.J. and **Maulik P.** (2011) Abraded sand volcanoes as a tool for recognizing paleo-earthquakes, with examples from the Cisuralian Talchir Formation near Angul (Orissa, eastern India). *Sedimentary Geology*, **238**, 145-155.

Van Loon, A.J., Pisarska-Jamroży, M., Nartišs, M., Krievāns, M. and **Soms, J.** (2016) Seismites resulting from high-frequency, high-magnitude earthquakes in Latvia caused by Late Glacial glacio-isostatic uplift. *Journal of Palaeogeography*, **5**, 363-380.

Van Loon, A.J., Pisarska-Jamroży, M. and **Woronko, B.** (2020) Sedimentological distinction in glacigenic sediments between load casts induced by periglacial pro cesses from those induced by seismic shocks. *Geological Quarterly*, **64**. http://dx.doi.org/10.7306/gq.1546

Van Vliet-Lanoë, B., Magyari, A. and **Meilliez, F.** (2004) Distinguishing between tectonic and periglacial deformations of quaternary continental deposits in Europe. *Global and Planetary Change*, **43**, 103-127.

Vanneste, K., Meghraoui, M. and **Camelbeeck, T.** (1999) Late Quaternary earthquake-related soft-sediment deformation along the Belgian portion of the Feldbiss Fault, Lower Rhine Graben system. *Tectonophysics*, **309**, 57-79.

Vanneste, K., Mees, F. and **Verbeeck, K.** (2008) Thin-section analysis as a tool to aid identification of palaeoearthquakes on the “slow”, active Geleen Fault, Roer Valley Graben. *Tectonophysics*, **453**, 94-109.

Wheeler, R.L. (2002) Distinguishing seismic from nonseismic soft-sediment structures: criteria from seismic-hazard analysis. In: *Ancient Seismites* (Eds. F.R. Ettensohn, N. Rast and C.E. Brett), *GSA Special Paper*, **359**, 1-11.

Woźniak, P.P., Belzyt, S., Pisarska-Jamroży, M., Lamsters, K., Nartisš, M. and **Woronko, B.** (2019) Pleistocene glaciolacustrine sediments with multiple, sandwich-like deformed layers (Baltic Sea bluff at Baltmuiža, western Latvia). *INQUA Congress 25–31.07.2019, Dublin, Ireland. Abstract book*. P-2827.

Zhong, N., Li, H., Jiang, H., Lu, H., Zheng, Y., Han, S. and **Ye, J.** (2020) Typical soft–sediment deformation structures induced by freeze/thaw cycles: a case study of Quaternary alluvial deposits in the Northern Qiangtang Basin, Tibetan Plateau. *Acta Geologica Sinica (English Edition)*, **95**, 176-188.

Zieliński, T. and **Van Loon, A.J.** (1999) Subaerial terminoglacial fans II: a semi-quantitative sedimentological analysis of the middle and distal environment. *Geologie en Mijnouw*, **78**, 73-85.

Zieliński, T. and **Pisarska-Jamroży, M.** (2012) Jakie cechy litologiczne osadów warto kodować, a jakie nie? [Which features of deposits should be included in a code and which not?] *Przegląd Geologiczny [Geological Review]* **60**, 387-397. [in Polish with English abstract]

[Figure captions],

Fig. 1. Study area. A: Location of the Dyburiai site in north-western Lithuania. B: Geological map of the study area (modified after Jusienė, 2012).

Fig. 2. General view of the outcrop at the Dyburiai site. A: Location of the outcrop at the steep bank of the Minija River valley. B: View of lacustrine sediment layers with SSDS interbedded with undeformed sediments. Major faults and joints are marked by white lines.

Fig. 3. Sediment succession at the Dyburiai site. A: Sedimentary units (1-4), lithofacies (code explained in the legend), OSL ages, and petrographic composition of gravel fraction in tills (after Jusienė, 2012 and Pisarska-Jamroży *et al*., 2018b). B: Sediment layers with SSDS and erosional features in the SW part of outcrop (note lack of layer SSDS-2) with locations of samples used for thin section production (Di1A-Di10).

Fig. 4. Sediments in the SW part of the section (see Fig. 2A). A: A sandwich-like/pancake arrangement of deformed (SSDS-3–10) and undeformed layers. Note the lateral continuity of most of the layers with SSDS. B: Close-up view of layers SSDS-8, -9 and -10 interbedded with layers of ripple cross-laminated fine sand and silt. C: Close-up view of layers SSDS-3 and -4 interbedded with thin undeformed sediments (lower part of photo). Sediment injection into layer SSDS-6 and into the overlying low-angle cross-stratified sand (upper part of photo).

Fig. 5. Soft-sediment deformation structures in the lacustrine sediment succession and their distribution in layers SSDS-1 to -10 (not to scale).

Fig. 6. Load structures. A: Loaded fine sand accompanied by injected sandy silt. B: Sandy drop-shaped load casts within layer SSDS-10. C: Detached and rotated ball-and-pillow structure within sandy silt (NE part of layer SSDS-1). D: Layer SSDS-1 with load casts and pseudonodules (resulting from different stages of loading), and fragments of broken-up-laminae (SW part of the section). Note the different sizes, shapes and internal secondary deformations of load structures, and the erosional top boundary of the layer with clayey clasts (upper part of the photo). E: Load cast of type C with eroded upper part separated from the overlying ripple cross-laminated sand. The internal primary lamination within the load cast is preserved (layer SSDS-1). F: Small-scale load casts and pseudonodules within layers SSDS-3

Fig. 7. Injection structures (direction of injection is marked by white arrows; loading direction by black arrows). A: Liquefied sediments from layer SSDS-5 cutting the overlying layer SSDS-6, the primarily horizontally-laminated sands, the layer SSDS-7 and the injecting sediments at the contemporary lake bottom surface (palaeosurface). B: View showing the relation between the liquefied injected sediment (internally deformed silt and sandy silt) and the hosting fine sand. C: Small-scale injections of sandy silt into silty sand host sediment (layer SSDS-5 in the NE part of the section). Faults displacing previously deformed sediments are marked with white lines. D: Injection of liquefied sand with ripple-cross lamination accompanied by load structures (layer SSDS-2, NE part of the section). Note that the low-permeability clayey laminae determine the upper boundary of the liquefaction front. E: Small-scale injection structures within layer SSDS-9.

Fig. 8. Grain size analysis of sediment layers with SSDS. A: Cumulative grain-size distribution curves of injected sediments (dashed lines) and loaded sediments (solid lines). B: Median diameters of injected and loaded sediments. C: Distribution of sorting parameters in

injected sediments (dashed lines) and loaded sediments (solid lines). Note that the injected sediments are somewhat finer-grained and less well sorted than the loaded sediments.

Fig. 9. Fragments of broken-up laminae. A: Sandy, detached fragments of laminae suggesting rapid injection of silty sand (layer SSDS-1). B: Fragments of sandy laminae in layer SSDS-10. C: Broken-up laminae in layer SSDS-8. Note the curved, almost vertical laminae on the left side of the panel as well as horizontally oriented laminae on the right.

Fig. 10. Brittle deformations cutting the layers with older SSDS. Faults are marked with white lines. A: Dense network of two sets of nearly vertical conjugate hybrid faults. Note the displacement of previously deformed SSDS layers. A': Contour diagram of poles of 30 fault planes with mean planes orientation for each of fault sets and the orientation of principal stresses (σ_1 = 258°/75° is nearly vertical; lower hemisphere projection). B: 3D intersection with faults cutting layers SSDS-8, -9 and -10. C-D: Disintegrated and displaced angular (trapezoid shape) clasts of layer SSDS-8, with well-preserved internally deformed structure, in a massive sandy and silty matrix.

Fig. 11. Thin section views (left) and interpretations (right). A: Sample Di1A (layer SSDS-1). B: Sample Di1B (uppermost part of layer SSDS-1). See Fig. 3B for location of the thin section. Also marked are locations of photomicrographs shown in Fig. 13.

Fig. 12. Thin section views (left) and interpretations (right). A: Sample Di3 (layer SSDS-30). B: Sample Di10 (layer SSDS-10). See Fig. 3B for location of the thin section. Also marked are locations of photomicrographs show in Fig. 13.

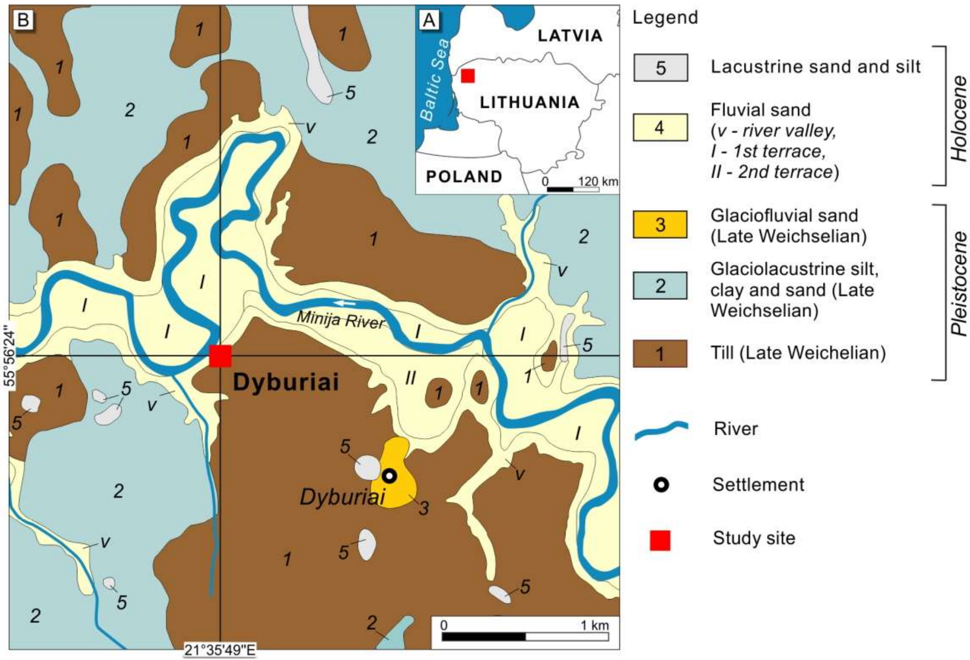

Fig. 1. Study area. A: Location of the Dyburiai site in north-western Lithuania. B: Geological map of the study area (modified after Jusienė, 2012).

Fig. 2. General view of the outcrop at the Dyburiai site. A: Location of the outcrop at the steep bank of the Minija River valley. B: View of lacustrine sediment layers with SSDS interbedded with undeformed sediments. Major faults and joints are marked by white lines.

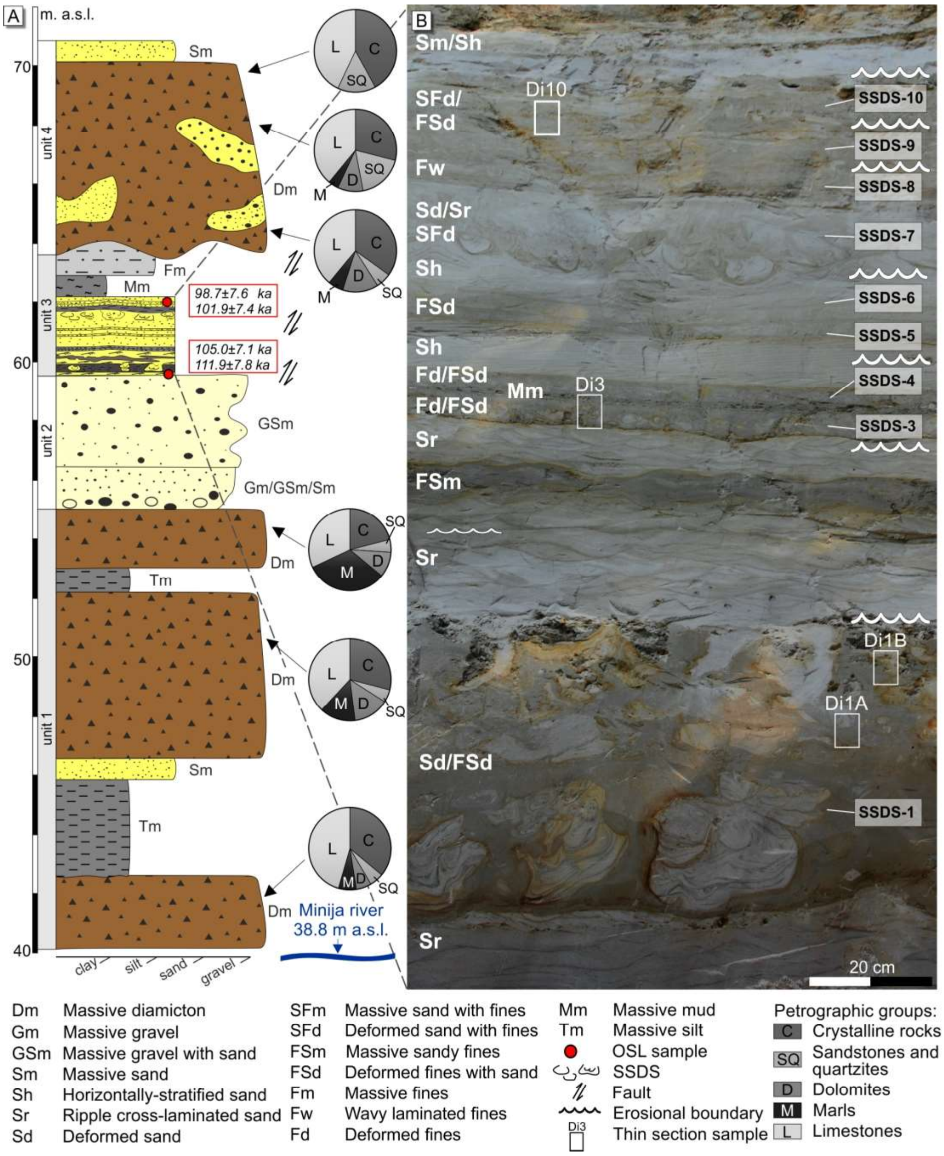

Fig. 3. Sediment succession at the Dyburiai site. A: Sedimentary units (1-4), lithofacies (code explained in the legend), and OSL ages, and petrographic composition of gravel fraction in tills (after Jusienė, 2012 and Pisarska-Jamroży et al., 2018b). B: Sediment layers with SSDS and erosional features in the SW part of outcrop (note lack of layer SSDS-2) with locations of samples used for thin section production (Di1A-Di10).

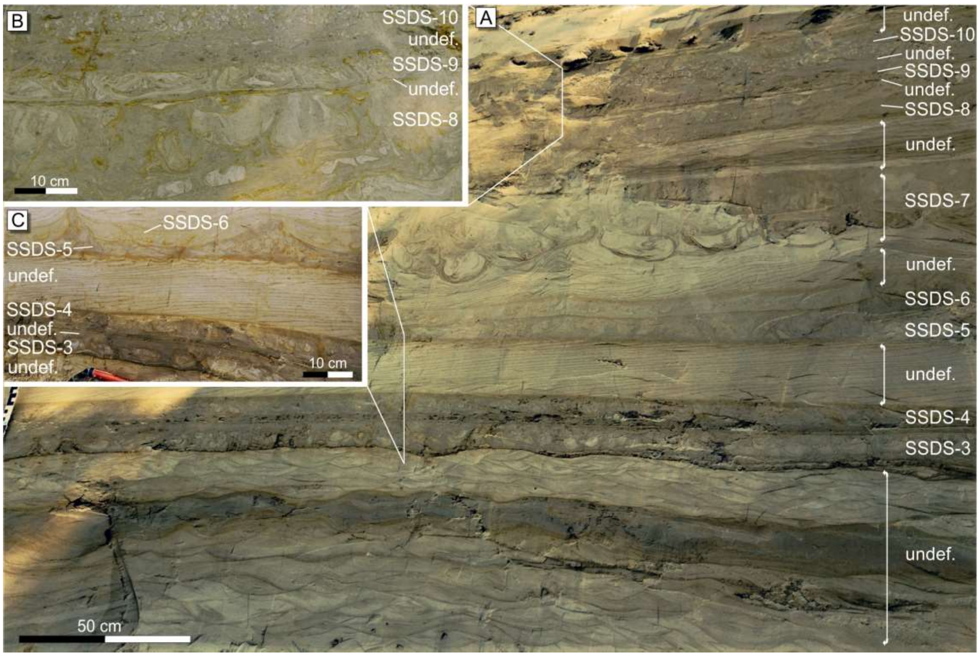

Fig. 4. Sediments in the SW part of the section (see Fig. 2A). A: A sandwich-like/pancake arrangement of deformed (SSDS-3–10) and undeformed layers. Note the lateral continuity of most of the layers with SSDS. B: Close-up view of layers SSDS-8, -9 and -10 interbedded with layers of ripple cross-laminated fine sand and silt. C: Close up view of layers SSDS-3 and -4 interbedded with thin undeformed sediments (lower part of photo). Sediment injection into layer SSDS-6 and into the overlying low-angle cross-stratified sand (upper part of photo).

SSDS layer no.	load casts A		load casts B	load casts C	pseudonodules	ball-and-pillow structures	broken-up laminae	injections
	teardrop	flat-bottommed	complex					
10	✓	✓	✓	✓	✓			✓
9			✓		✓	✓		✓
8		✓	✓		✓		✓	✓
7			✓					✓
6		✓	✓					✓
5		✓	✓					✓
4		✓			✓			✓
3		✓			✓			✓
2			✓					✓
1		✓	✓	✓	✓	✓	✓	✓

Fig. 5. Soft-sediment deformation structures in the lacustrine sediment succession and their distribution in layers SSDS-1 to -10 (not to scale).

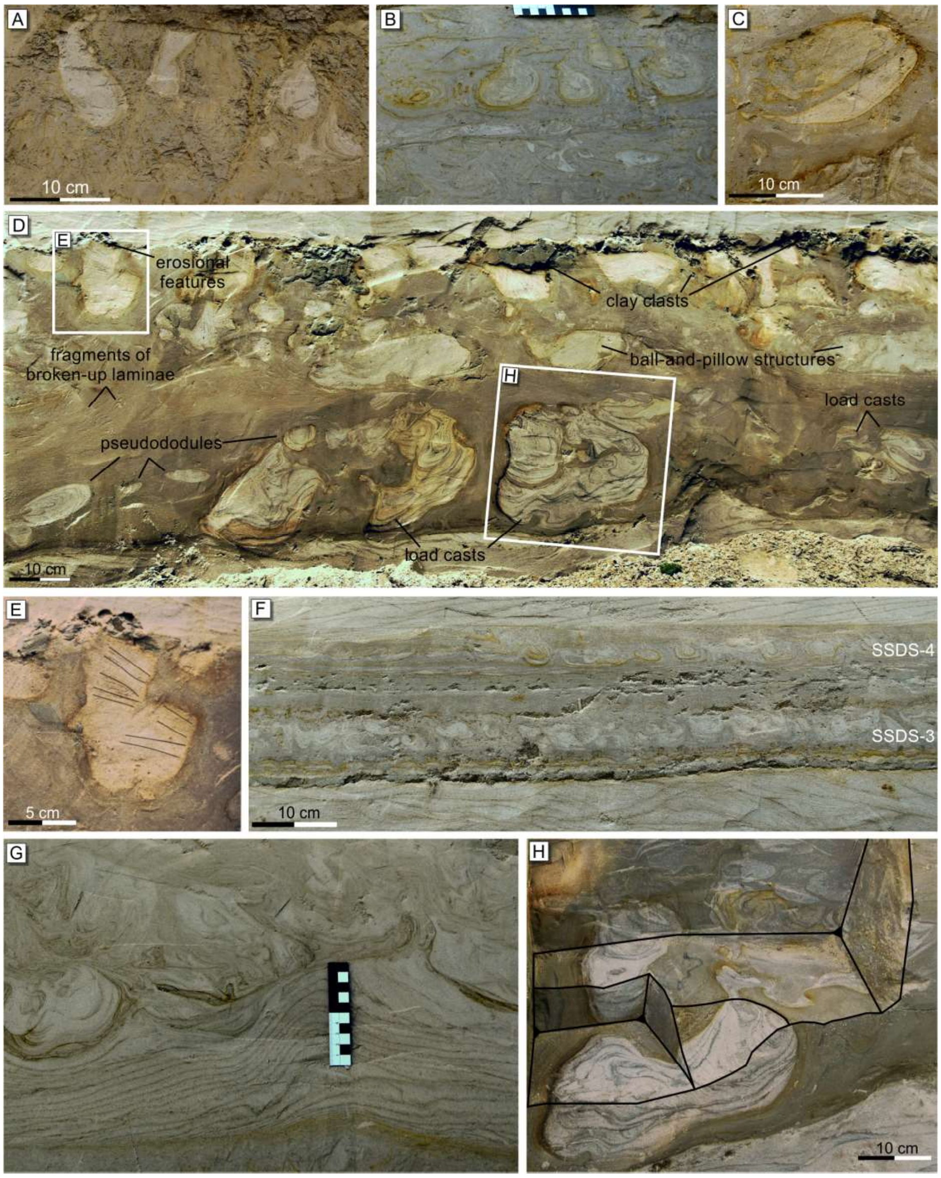

Fig. 6. Load structures. A: Loaded fine sand accompanied by injected sandy silt. B: Sandy drop-shaped load casts within layer SSDS-10. C: Detached and rotated ball-and-pillow structure within sandy silt (NE part of layer SSDS-1). D: Layer SSDS-1 with load casts and pseudonodules (resulting from different stages of loading), and fragments of broken up-laminae (SW part of the section). Note the different sizes, shapes and internal secondary deformations of load structures, and the erosional top boundary of the layer with clayey clasts (upper part of the photo). E: Load cast of type C with eroded upper part separated from the overlying ripple cross-laminated sand. The internal primary lamination within the load cast is preserved (layer SSDS-1). F: Small-scale load casts and pseudonodules within layers SSDS-3

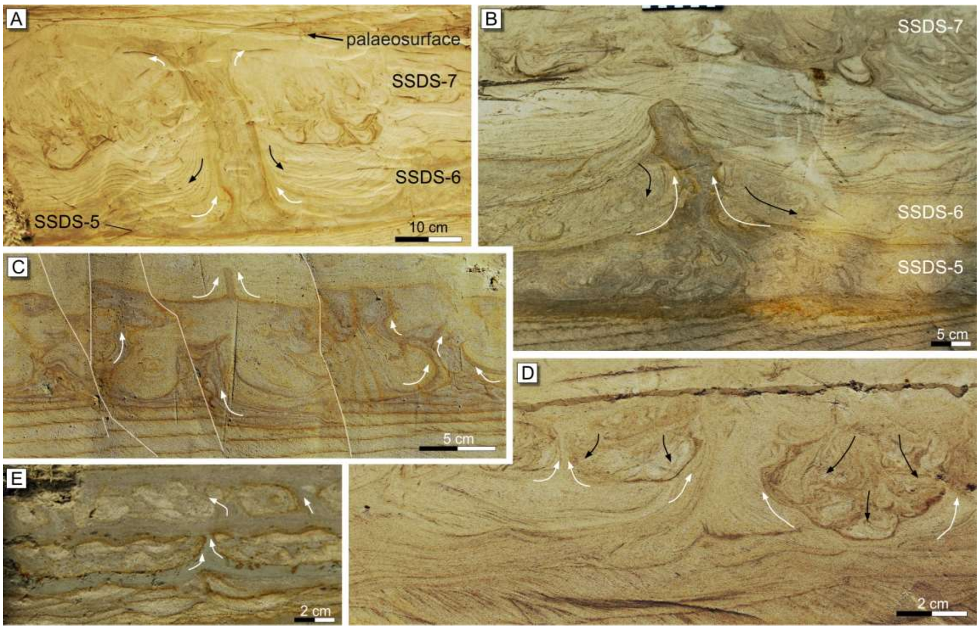

Fig. 7. Injection structures (direction of injection is marked by white arrows; loading direction by black arrows). A: Liquefied sediments from layer SSDS-5 cutting the overlying layer SSDS-6, the primarily horizontally-laminated sands, the layer SSDS-7 and the injecting sediments at the contemporary lake bottom surface (palaeosurface). B: View showing the relation between the liquefied injected sediment (internally deformed silt and sandy silt) and the hosting fine sand. C: Small-scale injections of sandy silt into silty sand host sediment (layer SSDS-5 in the NE part of the section). Faults displacing previously deformed sediments are marked with white lines. D: Injection of liquefied sand with ripple-cross lamination accompanied by load structures (layer SSDS-2, NE part of the section). Note that the low-permeability clayey laminae determine the upper boundary of the liquefaction front. E: Small-scale injection structures within layer SSDS-9.

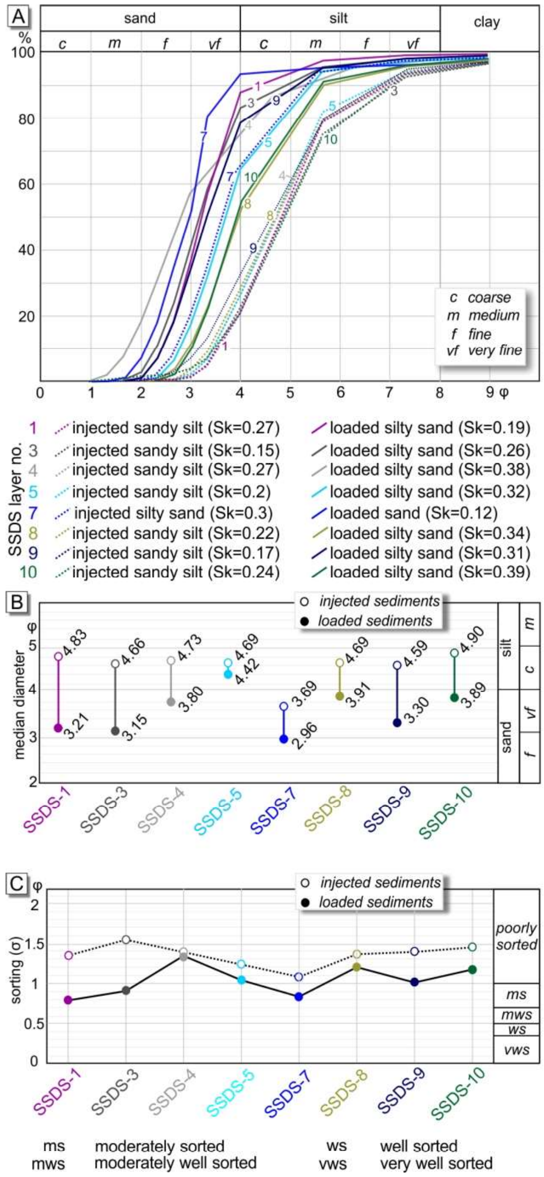

Fig. 8. Grain size analysis of sediment layers with SSDS. A: Cumulative grain-size distribution curves of injected sediments (dashed lines) and loaded sediments (solid lines). B: Median diameters of injected and loaded sediments. C: Distribution of sorting parameters in injected sediments (dashed lines) and loaded sediments (solid lines). Note that the injected sediments are somewhat finer-grained and less well sorted than the loaded sediments.

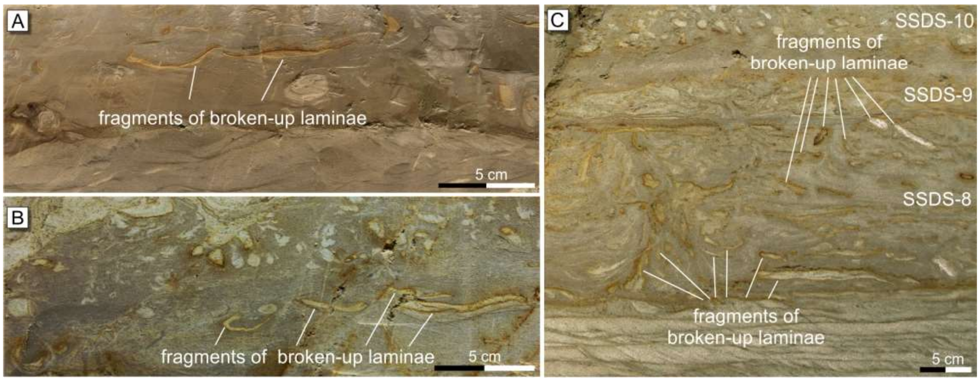

Fig. 9. Fragments of broken-up laminae. A: Sandy, detached fragments of laminae suggesting rapid injection of silty sand (layer SSDS-1). B: Fragments of sandy laminae in layer SSDS-10. C: Broken-up laminae in layer SSDS-8. Note the curved, almost vertical laminae on the left side of the panel as well as horizontally oriented laminae on the right.

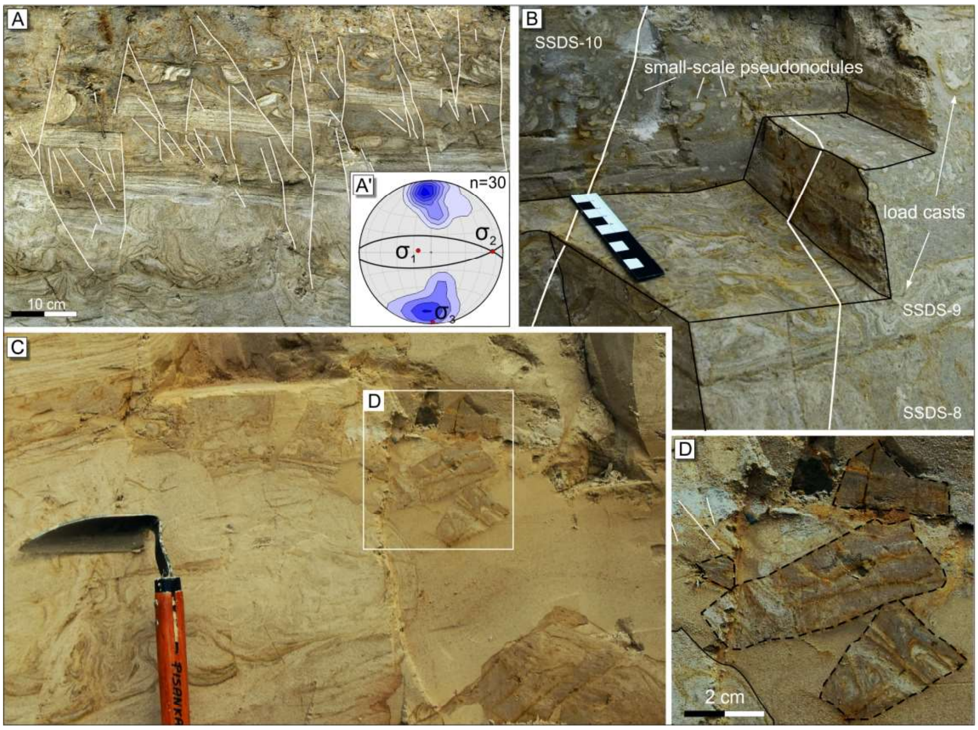

Fig. 10. Brittle deformations cutting the layers with older SSDS. Faults are marked with white lines. A: Dense network of two sets of nearly vertical conjugate hybrid faults. Note the displacement of previously deformed SSDS layers. A': Contour diagram of poles of 30 fault planes with mean planes orientation for each of fault sets and the orientation of principal stresses ($\sigma1$ = 258°/75° is nearly vertical; lower hemisphere projection). B: 3D intersection with faults cutting layers SSDS-8, -9 and -10. C-D: Disintegrated and displaced angular (trapezoid shape) clasts of layer SSDS-8, with well-preserved internally deformed structure, in a massive sandy and silty matrix.

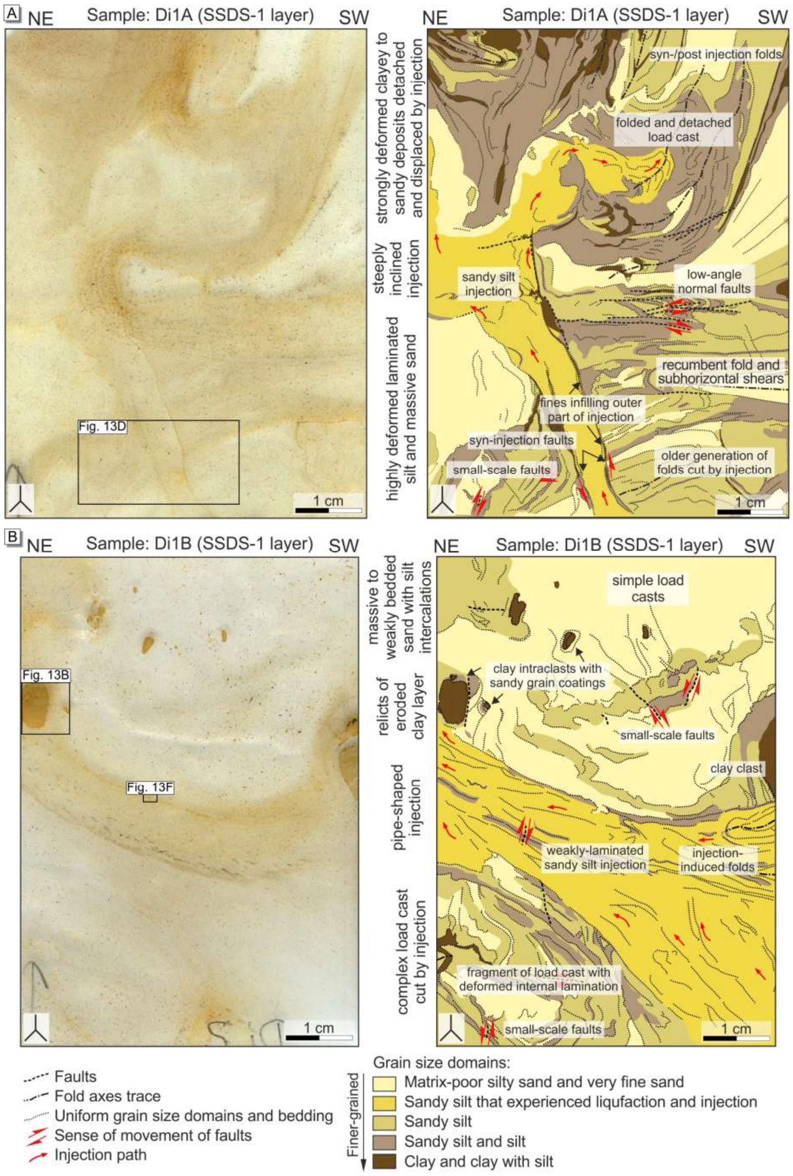

Fig. 11. Thin section views (left) and interpretations (right). A: Sample Di1A (layer SSDS-1). B: Sample Di1B (uppermost part of layer SSDS-1). See Fig. 3B for location of the thin section. Also marked are locations of photomicrographs shown in Fig. 13.

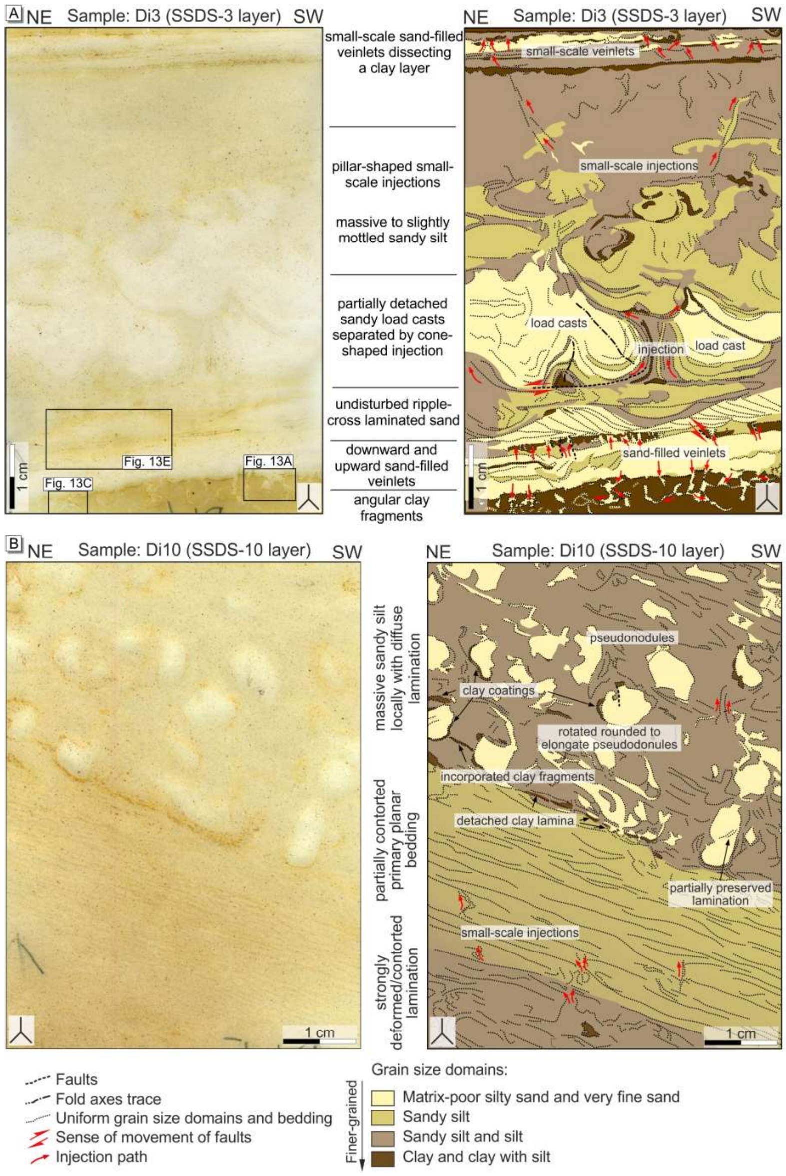

Fig. 12. Thin section views (left) and interpretations (right). A: Sample Di3 (layer SSDS-30). B: Sample Di10 (layer SSDS-10). See Fig. 3B for location of the thin section. Also marked are locations of photomicrographs show in Fig. 13.

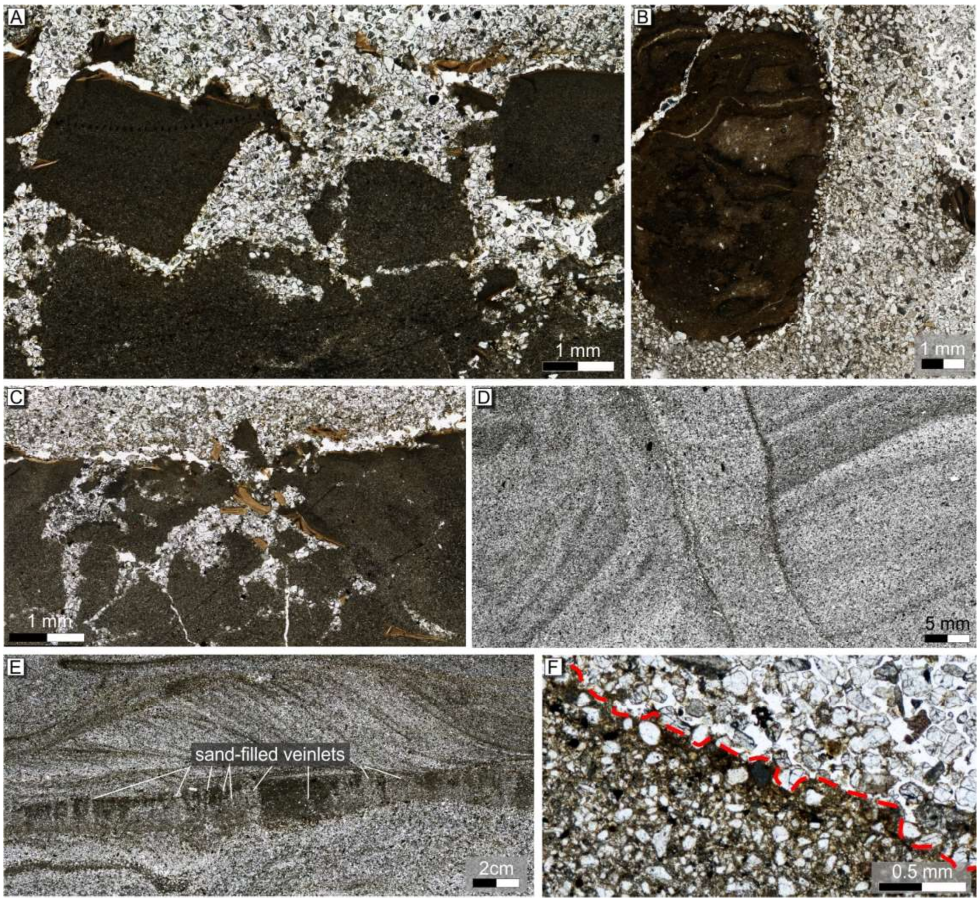

Fig. 13. Photomicrographs of samples Di1A, Di1B and Di3. A: Angular clay fragments resulting from downward injection of sand-filled veinlets (lowermost part of sample Di3, plane polarized light (PPL)). B: Clay clast with sand-grain coating (sample Di1B, PPL). C: Sand-filled veinlets injected into clay (lowermost part of sample Di3, PPL). D: Injection dyke with fines along its margins cutting the planar-bedded and deformed host sediments (sample Di1A, PPL). Note the massive structure of the injection dyke. E: Minute sand-filled veinlets in clay with upward sense of sand advection directly overlain by a cross-laminated undisturbed ripple (lower part of sample Di3, PPL). F: Boundary between injected (upper part) and host sediments (lower part) highlighted by a grain size boundary marked by red dotted line (sample Di1B, PPL).

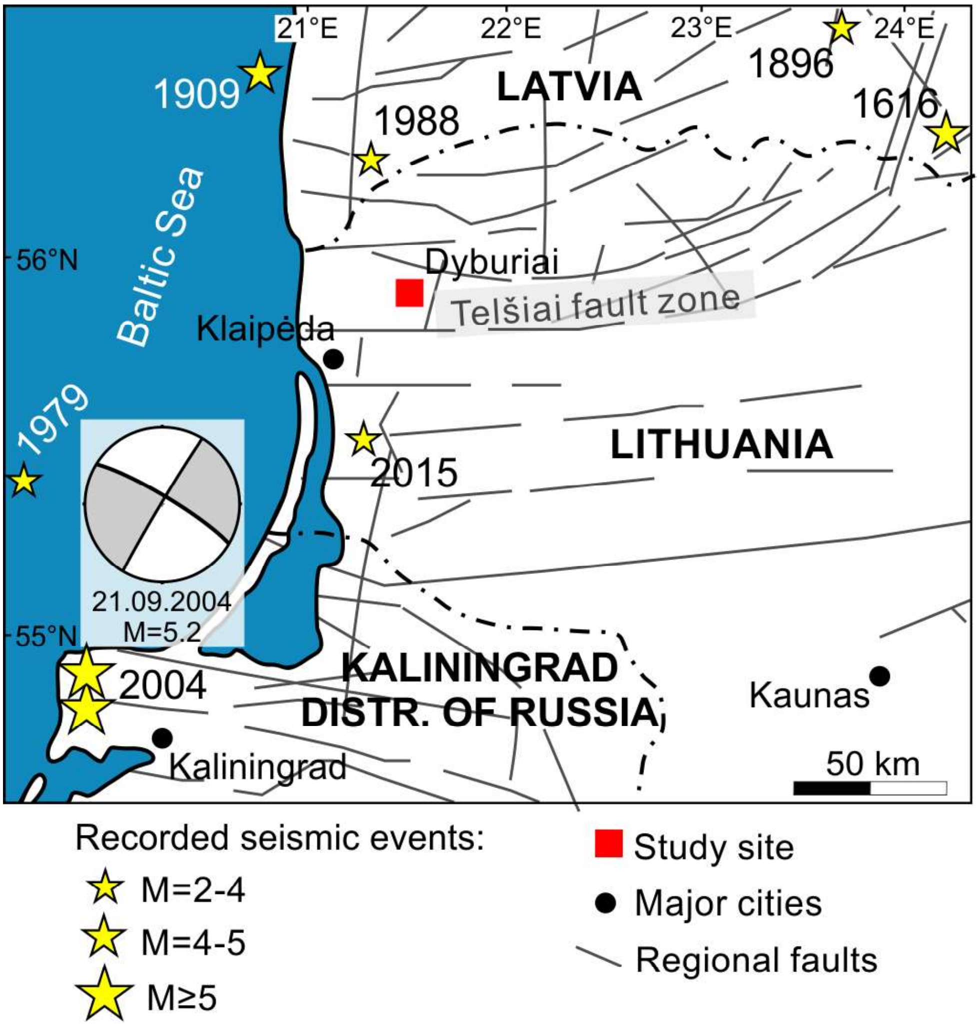

Fig. 14. Regional faults and seismic events in the south-eastern Baltic region (after Gregersen et al., 2007; Pačėsa & Šliaupa, 2011; Lazauskienė et al., 2012; Nikulins & Assinovskaya, 2018).

SSDS layer no.	features of layer			features of SSDS within layer			
	thic-kness (cm)	boundaries (B-base, T-top)	others	SSDS type	sediment: host	sediment: fill	ratio of SSDS size to layer thickness
7th palaeosurface during liquefaction event					sandy silt		
10	20-25	T - erosional; B – gradational	cut by faults	pseudonodules, load casts (type A, B), fragments of broken-up laminae	sandy silt	silty sand	sublayers with small scale pseudonodules and (locally) load casts
6th palaeosurface during liquefaction event					sandy silt		
9	5-7	T - erosional; B – gradational	cut by faults	load casts (type B), injection structures,	sandy silt	silty sand	variable size of SSDS (Fig. 10B)
5th palaeosurface during liquefaction event					sandy silt	silty sand	
8	10-25	T - erosional; B – gradational	cut by faults	load casts (type A, B), pseudonodules, fragments of broken-up laminae, injection structures (Fig. 9C)	sandy silt	silty sand	chaotically distributed sublayers of SSDS (⌀ not exceeding 8 cm; Fig. 9C)
4th palaeosurface during liquefaction event					sandy silt		
7	10-35	T – unclear, partially erosional, B – gradational (irregular, undulated)	thickness is changing; cut by injections rooted in SSDS-5	load casts (type B), flame structures	fine sand	silty sand	SSDS of variable size are irregularly distributed along the vertical extent
6	8	T- erosional; B- gradational	cut by injections rooted in SSDS-5	load casts (type A, B) injection structures (Fig. 6B)	sandy silt	silty sand	sublayers of irregularly distributed small-scale load casts (1-5 cm)
5	10	T- gradational; B- erosional	injection structures cut the overlying sediments (Fig. 6A, B)	load casts (type A,B), injection structures (Fig. 6A-C), less frequent in SW part	sandy silt	silty sand	two or three sublayers of irregularly distributed small-scale load casts (1-5 cm); injections cutting the whole overlying SSDS-6 and part of SSDS-7
3rd palaeosurface during liquefaction event					sandy silt	silty sand	
4	5-7	T- erosional (sharp); B- gradational	both layers SSDS-3 and SSDS-4 merge and create one 12-cm-thick layer in NE part of the section	injection structures, load casts (type A), flame structures, pseudonodules; all in small-scale (Fig. 8F)	sandy silt	silty sand	one dominant layer with SSDS accompanied by small-scale sublayers; all affecting the whole vertical extent; load casts diameter is up to 6x5 cm
3	5-7	T- gradational (sharp); B- gradational			sandy silt	silty sand	
2nd palaeosurface during liquefaction event					sandy silt		
2	0-25	T-erosional (sharp); B- gradational	present only in NE part; multiple stages of load casts formation (Fig. 6D)	vertical injection structures and load casts (type B); occurring at one level (Fig. 6D)	sandy silt	silty sand with lamin ae of sandy silt	one level with SSDS affecting the whole vertical extent
1st palaeosurface during liquefaction event					sandy silt		
1	25-50	T- erosional (silty clasts); B- gradational	thickness decreasing to the NE; clay clasts in upper part; some of load casts are strongly rotated	load casts, pseudonodules, balls-and-pillows, injection structures, fragments of broken-up laminae	sandy silt	silty sand	two to three irregularly distributed sublayers with SSDS; diameter of SSDS from 0.5 cm (pseudonodules) to 15 cm (ball-and-pillow structures)

Lower part of the succession (undisturbed sediments underlying the SSDS-1 layer)

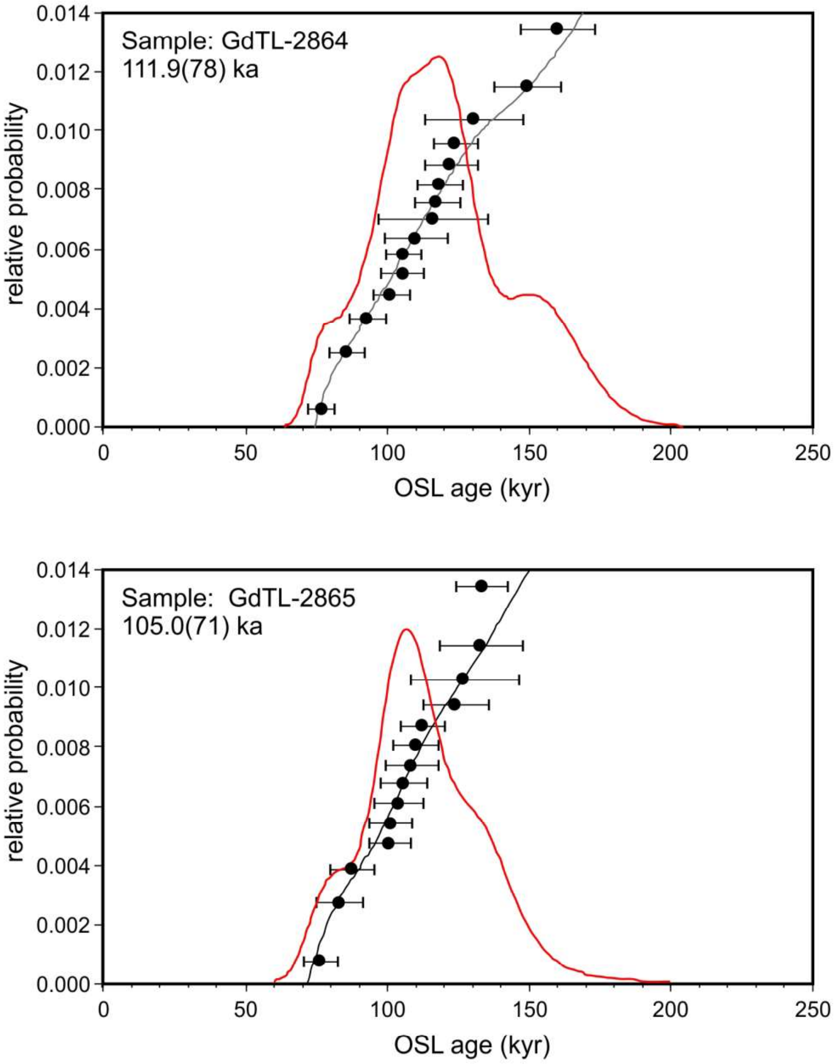

Upper part of the succession (undisturbed sediments overlying the SSDS-10 layer)